Finite element modelling of mixed-mode delamination propagation in Abaqus/Explicit with linear and nonlinear cohesive softening laws

Theo A. Rulko*, Minh Hoang Nguyen† and Anthony M. Waas‡
University of Michigan, Ann Arbor, MI, 48109, USA

Accurate modelling of delamination propagation in laminates is key to predicting the failure of composite structures. In this study, an implementation of the Cohesive Zone Model (CZM) using a novel mixed-mode formulation based on defining an effective separation and allowing for generalizable non-linear cohesive traction-separation softening laws, is presented and evaluated. To this end, several finite element models representing a laminate specimen under pure mode I, pure mode II, or mixed-mode conditions, respectively, are constructed and benchmarked against other studies from literature. Then, the influence of the cohesive softening law shapes on the load-displacement response of the specimen is evaluated. Results show that, with the appropriate softening law shape, the novel implementation successfully captures delamination growth and most load-displacement characteristics without the need for an empirical energy criterion.

I. Introduction & Background

Laminate composites are made up of several layers, or laminae, bonded together. They are widely used in the aerospace and automotive industries for their good elastic modulus, generally high strength-to-weight ratio, and the ability to be highly customized to fit a particular application. The ability to model how such a material will deform under load and how or when it will fail is extremely important to making it practical for widespread use. However, predicting the failure of laminate structures is difficult because of their complicated failure modes, which include both intra-laminar crack initiation and propagation in the fibers or matrix, fiber kinking and rupture, inter-laminar delamination, and more, as shown in Fig. 1. Thus, though it is possible for these individual failure modes to interact, the study of the failure of laminate composites is generally separated into the study of each.

The focus of this particular study is on the onset and propagation of delamination, which is a predominant failure mode in laminates where a crack forms and propagates between plies and they de-bond. Delamination is especially common when the material is subjected to bending, in-plane compression, and other loads, and is often initiated at defects present in the material which act as stress concentrators, or by external events such as an impact [1]. There is great research interest in cohesive modeling of delamination initiation and propagation [2–13].

Generally, delamination is driven by interlaminar normal stress (mode I) and interlaminar shear stresses (mode II and III). To predict the initiation of a crack from which the delamination propagates, various

*Undergraduate Research Assistant (Honors Capstone), Department of Aerospace Engineering, trulko@umich.edu.
†Graduate Research Assistant, Department of Aerospace Engineering, mhoangn@umich.edu.
‡Richard A. Auhll Department Chair, Felix Pawlowski Collegiate Professor, Department of Aerospace Engineering, awaas@umich.edu.

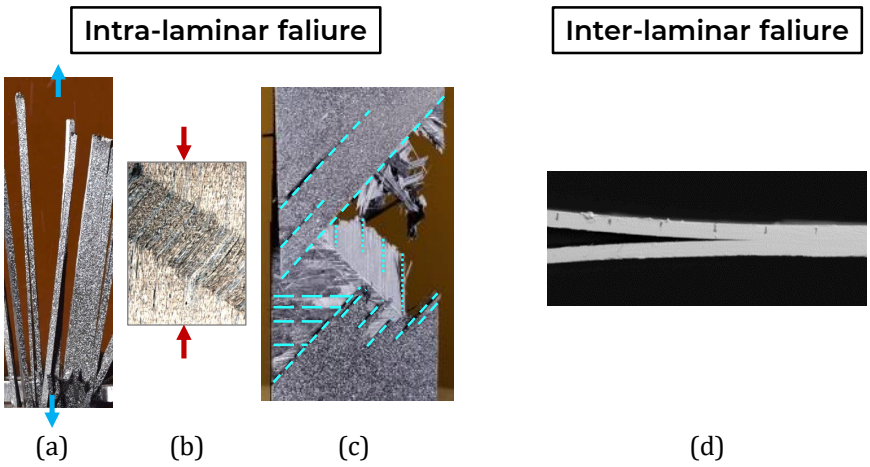

Fig. 1 Images of inter- and intra-laminar failure modes. Examples of (a) fiber rupture, (b) fiber kinking, (c) matrix failure, and (d) delamination, are shown. These failure types can interact in a real-world scenario.

techniques using critical values of field variables like stress in the plies themselves are used [4]. To predict crack growth and propagation, a different set of techniques are used, based on fracture mechanics and the energy release rate G as the crack propagates. These include the Virtual Crack Closure Technique (VCCT) and the Cohesive Zone Model (CZM).

VCCT was first developed by Rybicki and Kanninen in 1977 [14]. This method relies on the notion that the energy released when the crack propagates by an infinitesimal amount is equal to the work required to close the crack. However, this method often requires a moving mesh technique to accurately capture the delamination front, meaning it often requires a non-standard FEM implementation of great complexity. Further disadvantages include that it cannot simulate a non-self-similar delamination front, though delamination fronts are rarely self-similar [15], and that for VCCT, a pre-crack is required, so crack initiation cannot be simulated.

CZM was proposed by Dudgale-Barenblatt in 1960 [16]. In this technique, special non-linear so-called cohesive finite elements are used at the interface between solid finite elements to model initiation and non-self-similar growth of delamination. In this method, the beginning of the softening process and eventual failure of individual cohesive elements are predicted using a combination strength-based approach and fracture mechanics. A cohesive law dictates the behavior and represents the local traction versus the crack opening displacement. The traction across the crack interface increases elastically with displacement until it reaches a critical value where it satisfies a failure criterion, then decreases until it eventually vanishes, allowing the element to fail and the crack to propagate (see Fig. 3). The cohesive elements themselves represent the matrix-rich layer between the plies and are therefore considered to be a realistic representation of the delamination process, because they contain the softening behavior to a very thin layer between the plies. Compared to the VCCT model, the CZM model removes the occurrence of a stress singularity at the tip of the crack. In CZM, the crack growth and resulting load-displacement response of the specimen depend on the initial delamination length, cohesive properties, the shape of the traction-separation laws, and the mode mixity ratio [4].

In this study, the CZM method is used to model delamination behavior, and the effects of each of the aforementioned parameters on the specimen behavior are studied.

A. Test apparatus

Several widely used experimental techniques to characterize delamination and measure interface properties have been established and standardized, including the Double Cantilever Beam (DCB), End Notched Flexure (ENF), and Mixed Mode Bending (MMB) tests, described in ASTM-D5528 [17], ASTM-D7905 [18], and ASTM-D6671 [19], respectively. Each of these tests is used to characterize the behavior of the specimen under different mode mixity ratios, defined as G_{II}/G_T where $G_T = G_I + G_{II}$. DCB and ENF tests are used for $G_{II}/G_T = 0\%$ or 100%, respectively, while the MMB test allows for a range of mode mixity ratios to be tested. The experimental apparatus used for these tests is highlighted in Fig. 2.

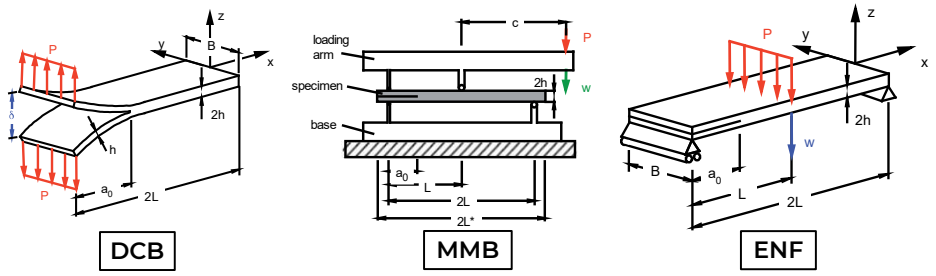

Fig. 2 ASTM-standard double cantilever beam (DCB), mixed-mode bending (MMB), and end notched flexure (ENF) experimental apparatus. [20]

B. The cohesive traction-separation law

The shape of the cohesive law plays a key role in the load-displacement behavior of a laminate specimen. Its shape can be arbitrarily complicated depending on the material and structural properties of the inter-laminar bond and its geometry. For example, any inhomogeneity in the ply-ply interface, such as gaps produced during automated fiber placement manufacturing or pores in the matrix material, can result in cohesive laws with sharp discontinuities [21]. In most implementations of CZM, however, the cohesive law is assumed to be triangular (Fig. 3 (a)), so that it can be defined by only three experimentally determined parameters for each mode: the cohesive strength σ_c, cohesive penalty stiffness K, and the critical fracture toughness G_c.

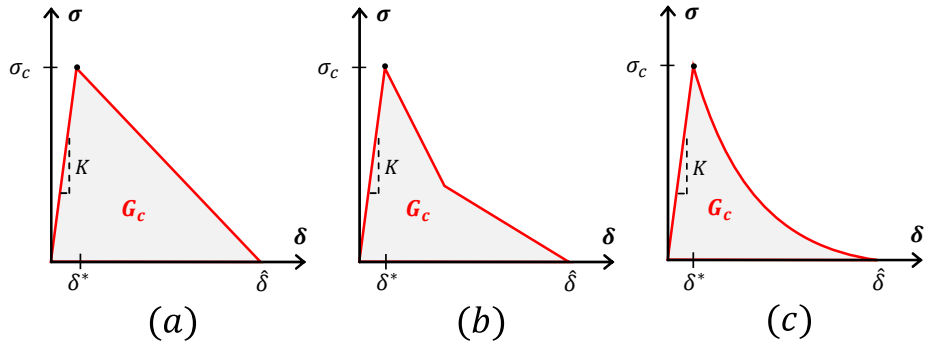

Fig. 3 Proposed (a) linear, (b) bilinear, and (c) exponential simplified cohesive softening law formulations.

In some rare, advanced models, laws have also been defined by a linear-elastic portion followed by a bilinear or exponential softening portion, as shown in Fig. 3 (b) and (c) [3, 5, 7, 21, 22]. In these cases, the additional information necessary to fit the law has occasionally been obtained experimentally [3, 21, 23].

For example, Girolamo et al., 2015 [3], have achieved this by measuring the displacement jump and precise rotation of the loading arms in the mode I and mode II loading apparatus, using stereoscopic digital image correlation (DIC) focused on the crack tip, and then working backwards from the obtained data with a non-linear fracture mechanics J-integral analysis approach to determine the pure-mode cohesive laws.

Regardless of how the shape of the law is controlled, the displacement at which the peak occurs can be determined using Eq. (1) below, and the displacement at which the element fails can be found by integrating the cohesive law such that Eq. (2) holds. K_i, δ_i^*, σ_c, $\widehat{\delta_i}$, σ, and δ are defined in Fig. 3 above.

$$\delta_i^* = \frac{\sigma_c}{K_i} \text{ for } i = I, II, III \tag{1}$$

$$G_{ic} \equiv \int_0^{\widehat{\delta_i}} \sigma_i \, d\delta_i \tag{2}$$

In this study, a different approach, where the cohesive softening law is parametrized by a Bezier curve, is presented and evaluated.

C. Determining the mixed-mode cohesive law

Beyond just geometric and material properties, the shape of the cohesive law is a function of how the specimen is loaded and may vary with the mode mixity ratio, G_{II}/G_T, where $G_T = G_{\text{I}} + G_{\text{II}}$. The pure mode cohesive properties when $G_{\text{II}}/G_T = 0\%$ or 100% can be measured experimentally for a given material with relative ease using ASTM-standard tests: the double-cantilever beam (DCB) test for pure mode I, and the end-notched flexure (ENF) test for pure mode II. Under mixed-mode loading conditions, where the mixity ratio is neither 0% nor 100%, softening and damage onset occur before the individual pure-mode traction components reach their respective critical fracture energies [1, 4].

Rather than experimentally characterizing the cohesive law for every possible mixity ratio, most CZM implementations use an empirical approximation to link the pure mode laws to a mixed-mode law. This is usually a linear, quadratic, or exponential rule fitted to experimental data to relate the pure-mode softening laws for use in a mixed-mode scenario. The two such rules which are most common include the Power Law criterion, proposed by Wu and Reuter in 1965 [24], and the Benzeggagh and Kenane (B-K) criterion [25], proposed in 1996.

The Power Law criterion is a two-parameter criterion defined according to Eq. (3) below, where the exponent α is a fitting parameter:

$$\left(\frac{G_{\text{I}}}{G_{\text{I}c}}\right)^{\alpha} + \left(\frac{G_{\text{II}}}{G_{\text{II}c}}\right)^{\alpha} = 1 \tag{3}$$

Extensive testing of laminates under mixed-mode conditions by Reeder, 2000 [26] found that the fitting parameter $\alpha = 1$ works well in most cases, but fails to capture the dependence of the mixed-mode critical fracture toughness on the mode mixity ratio for some materials.

The B-K criterion is a single-parameter criterion where mixed mode fracture toughness G_c varies as a function of mode mixity ratio (G_{I}/G_T) and is a function of the pure mode critical fracture toughness values $G_{\text{I}c}$ and $G_{\text{I}c}$ determined experimentally [20]. The B-K criterion is given in Eq. (4) below, where the exponent η is the curve-fitting parameter:

$$G_c = G_{Ic} + (G_{IIc} - G_{Ic}) \left(\frac{G_{II}}{G_T} \right)^{\eta} \tag{4}$$

While these two empirical rules yield useful results in most cases, they do not work for all materials and loading configurations [1]. Furthermore, they are fundamentally based on an approximation to experimental data, rather than on theory. In this study, an alternative to this empirical method is explored, where a cohesive mixed-mode interaction criterion is defined to predict the onset of softening in mixed-mode conditions.

Ultimately, this study seeks to build and test a series of finite element models which implement CZM across a range of mode mixity ratios, using the commercially available Abaqus finite-element structural simulation software. The purpose of the study is to use these models to study how the shapes of the cohesive softening laws for modes I, II, and III affect the delamination behavior and overall load-displacement response, and to test a novel mixed-mode interaction formulation which relies on the definition of an effective separation and generalizable softening shapes. The selection of material-specific parameters is also discussed.

D. Selecting benchmark results for verification of FE models

Throughout this study, the finite element models developed will be compared to a series of benchmarks developed by Krueger, 2015 [20]. Krueger generated a series of 2D FEM models of a specimen under different loading conditions and with varying initial crack lengths a_0, then used them to find the total energy release rate G_T as a function of a_0 and the applied displacement δ. Based on a linear fracture mechanics relationship, the critical load and critical opening displacements were found as a function of a_0 and δ using Eq. (5) below:

$$P_{crit} = P\sqrt{\frac{G_c}{G_T}}, \quad \delta_{crit} = \delta\sqrt{\frac{G_c}{G_T}} \tag{5}$$

Here, P and the ratio G_T/G_c were determined from the FEM results, where G_c is the mixed-mode fracture toughness determined using the B-K criterion. Finally, by plotting the points $(P_{crit},\ \delta_{crit})$ obtained for a range of a_0 and δ values and fitting a curve to these points, Krueger was able to obtain the benchmarks referred to throughout this study. Note that these benchmarks assume that the delamination front is straight, whereas it is really curved. This difference likely accounts for the small disparity seen between the benchmark results and those obtained from 3D FEM simulations later in this study.

II. Methods

For the development and verification of the FEM models presented above, three distinct Abaqus models representing rectangular two-ply carbon fiber/epoxy prepreg laminate specimens under different quasi-static loading conditions for different mode mixity ratios (G_{II}/G_T) were developed. The models are a pure mode I model ($G_{II}/G_T = 0\%$), a pure mode II model ($G_{II}/G_T = 100\%$), and a mixed-mode model, which load the specimen in pure opening mode, pure shear, and a mixture thereof, respectively. Each of these is designed to replicate the experimental apparatus of the corresponding test: the double-cantilever beam (DCB), end-notched flexure (ENF) or mixed-mode bending (MMB) test, respectively. The mixed-mode model can be used to test a range of mixity ratios by tweaking geometric parameters of the loading apparatus. In this study, the MMB model was used to test the ratios $G_{II}/G_T = 20\%, 50\%$, and 80%.

A. Construction of the FE models in Abaqus/CAE

Each model is composed of at least three distinct parts representing the top and bottom plies along with the cohesive layer used in this implementation of CZM, as shown in Fig. 4. They have an initial crack (a delaminated region between the two plies) of length a_0, from which the delamination propagates during the FE simulation.

Ply material and geometry: In each of the three models, the prepreg material and specimen geometry were chosen to be identical to that used in Krueger's benchmark model [20], to allow for later comparison. Fig. 4 calls out important specimen dimensions which are listed in Table 1. In the MMB model, the mixity ratio G_{II}/G_T is controlled by the length c of the lever arm according to the equation given Appendix A. The material properties used for each specimen are listed in Table 2.

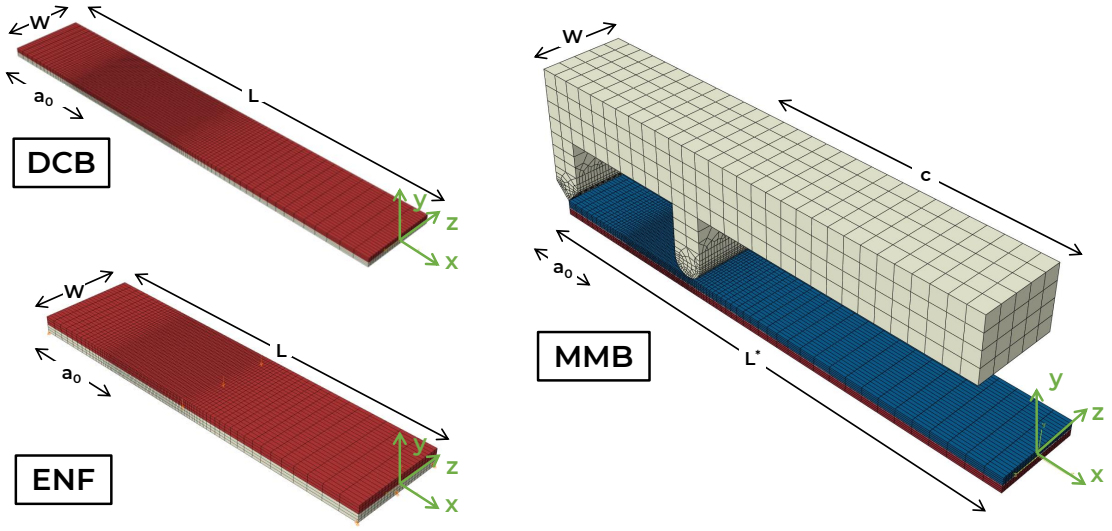

Fig. 4 Isometric views of each of the three models, showing the specimen and its dimensions, coordinate systems, and the MMB loading apparatus.

Table 1 Physical dimensions of the specimen in the DCB, ENF, and MMB models [20]

Dimension (mm)		DCB	ENF	MMB
Half-laminate thickness	H	1.5	2.25	2.25
Specimen Length	L	150	101.6	100.8
Specimen Total Length	L^*	-	-	152.4
Specimen Width	W	25	25.4	25.4
Initial Crack Length	a_0	30.5	25.4	25.4
Loading Arm Thickness	t	-	-	9.525
Loading Arm Length	c	-	-	92.9 mm for $G_{II}/G_T = 20\%$ 41.3 mm for $G_{II}/G_T = 50\%$ 27.3 mm for $G_{II}/G_T = 80\%$

Cohesive properties and layer geometry: In each model, a cohesive layer was modelled between the two plies with a thickness of 0.002 mm. This has been shown to not affect results compared to a zero-thickness

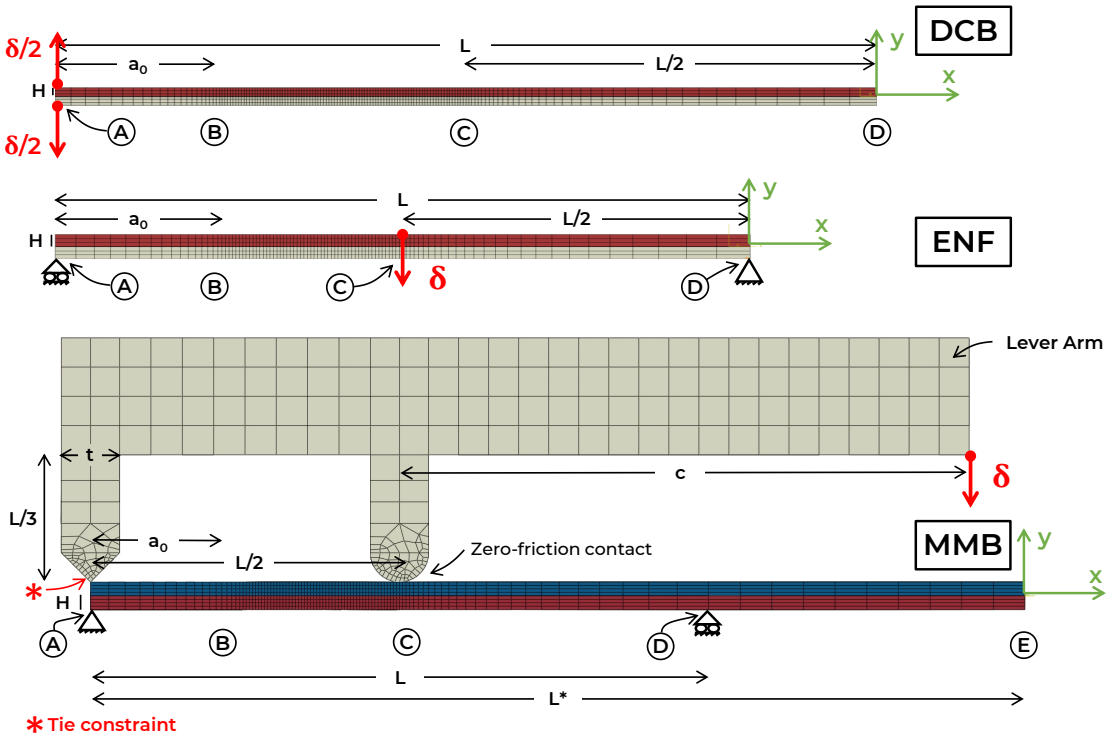

Fig. 5 Side views of the three models, showing geometry, dimensions, mesh, boundary conditions, and applied displacements.

layer, as demonstrated in Appendix B. The width of the cohesive layer was made identical to that of the plies, while its length is given by $L - a_0$, representing the bonded region of the interface between the plies. The non-bonded region of length a_0 represents the initial crack region from which the delamination propagates.

The density of the cohesive layer was set to 1.5E-09 tonnes/mm^3, the approximate density of epoxy [27]. The remaining cohesive properties for each model, including cohesive strength and stiffness, were not initially known. This is because material definitions were obtained from Krueger, 2015 [20], which uses VCCT rather than CZM. These properties were determined via a series of parametric studies described later in this report.

Meshing, Element Types, and Assembly: The laminae were meshed separately in Abaqus/CAE using C3D8I linear, explicit hex (8-node) elements, with a mesh as shown in Fig. 5. These elements were chosen as they allowed the plies to be meshed with rectangular prisms (bricks), were compatible with the explicit FEM solver used, and had yielded good results in various studies [20]. The mesh was made non-uniform in the lengthwise direction, so that it could be refined with a linear bias between control points in the delamination propagation region, to decrease simulation run time by decreasing the overall number of elements. The control points are indicated for each model by the circled letters in Fig. 5, with an element length of 3 mm at point A, 0.5 mm at point B and C, and 5 mm at point D and E (for MMB only). The elements were also modelled with a width of $W/25$ and a height of $H/3$, giving three elements through the thickness of each ply and 25 elements across their width, consistent with recommendations from literature to avoid problems with transitions between coarser and finer meshes reported by Krueger, 2015 [20].

The cohesive layer was meshed separately with COH3D8 linear, hex (8-node) elements using the built-in Abaqus/Explicit cohesive zone model. The element in-plane dimensions were made identical to those in the laminae (matching meshes), but with a thickness of 0.002 mm corresponding to the thickness of the layer.

Table 2 Carbon fiber/epoxy prepreg materials and their properties [20]

Material Property	DCB (T300/1076)	ENF, MMB (IM7/8552)
Density (tonne mm^{-3})	$\rho = 1.76 \times 10^{-9}$	$\rho = 1.76 \times 10^{-9}$
Young's Moduli (GPa)	$E_{11} = 139.4$	$E_{11} = 161$
	$E_{22} = E_{33} = 10.16$	$E_{22} = E_{33} = 11.38$
Poisson Ratios	$\nu_{12} = \nu_{13} = 0.30$	$\nu_{12} = \nu_{13} = 0.32$
	$\nu_{23} = 0.436$	$\nu_{23} = 0.45$
Shear Moduli (GPa)	$G_{12} = G_{13} = 4.6$	$G_{12} = G_{13} = 5.2$
	$G_{23} = 3.54$	$G_{23} = 3.9$
Coefficient of friction	$\mu = 0.3$	$\mu = 0.3$

This was done to ensure coincidence between nodes of the cohesive layer and upper and lower plies.

The two separately meshed plies and cohesive layer were assembled into a laminate, with the origin of the coordinate system centered vertically and widthwise and at the end of the laminate opposite the initial crack. Mesh orientation was assigned to be consistent between each part and with the global coordinate system. Tie constraints were added between each node on the top of the bottom ply and bottom of the cohesive layer, and between each node on the top of the cohesive layer and the bottom of the top ply, with both translational and rotational degrees of freedom tied. Finally, a global isotropic frictional interaction definition with a coefficient of friction of $\mu = 0.3$ was added between all surface pairs.

Boundary conditions & loading: Consistently with the experimental apparatus used in DCB, ENF, and MMB tests and described in ASTM-D5528 [17], ASTM-D7905 [18], and ASTM-D6671 [19], respectively, boundary conditions and displacements were applied to each model as shown in Fig. 5. As these tests are usually conducted in a tensile-test machine, time-varied displacement-controlled loading was used with a smooth step loading rate. The smooth step was defined between (0,0) and (2,2), as illustrated in Fig. 6, to ensure that the acceleration is always positive and to avoid inertia effects.

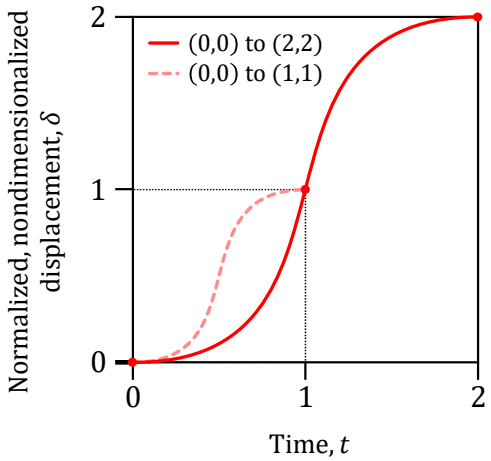

Fig. 6 Smooth step loading rate defined between $(0, 0)$ and $(1, 1)$ (dashed) or $(2, 2)$ (solid). In the latter case, acceleration is always positive.

In the DCB test, a displacement equal to $\delta/2$ was applied to each of the nodes on the top edge above

the initial crack, and a displacement of $-\delta/2$ was applied to each of the nodes on the bottom edge above the initial crack. Here, reaction forces from the applied displacement are balanced, so no additional boundary conditions were applied.

In the ENF test, an applied displacement of $-\delta$ was applied to a row of nodes in the middle of the top ply, at a distance $L/2$ from the end as shown in Fig. 5. A roller-type Dirichlet boundary condition was applied to the bottom-left end of the laminate, constraining vertical displacement, and a pin-type Dirichlet boundary condition was applied to the bottom-right end of the laminate, constraining vertical and horizontal displacement.

In the MMB test, a more complicated loading apparatus was used, consisting of the discretely modelled steel loading arm shown in Fig. 4 and 5. The apparatus was designed such that applying a downward load to the end of the lever results in an upward load on the end of the specimen, applying mode I loading, and a downward load to the center of the specimen, applying mode II loading. As per the ASTM standard [19], the height of the apparatus was set to $0.3L$ to keep non-linear geometric effects small, while its thickness t, given in Table 1, was approximated as the average thickness of the apparatus from the production drawings in the ASTM standard. To ensure that the center 'leg' (the fulcrum) allows sliding of the specimen, it has a zero-friction semi-circular end to approximate a roller. The other 'leg' ends in a point to approximate a pinned joint. A tie constraint was applied between that leg and the top ply of the specimen, tying the translational degrees of freedom between the apparatus and specimen, but allowing it to pivot freely. The approximate material properties of steel were used for the arm, including a density of ρ = 8E-09 tonne mm^{-3}, an isotropic Young's Modulus of E = 200 GPa, and Poisson's Ratio of ν = 0.25 [28]. The arm was meshed using a combination of linear explicit hexagonal (8-node) C3D8I, wedge (6-node) C3D6, and tetragonal (4-node) C3D4 elements to allow for the transition from a coarse cubical mesh in the lever arm to a finer, irregular mesh in the roller and pin.

Finally, an applied displacement of $-\delta$ was applied to the rear edge of the lever as indicated on Fig. 5 (MMB). As per the ASTM standard [19], a pin-type Dirichlet boundary condition was applied to the bottom-left end of the specimen, constraining vertical and horizontal displacement, and a roller-type Dirichlet boundary condition was applied at a distance L from the start of the specimen, constraining vertical displacement.

B. Mass Scaling

Variable mass scaling is used to decrease the computational time required for the models. A target stable time increment of 1E-06 seconds was used. Both larger and smaller stable time increments were also tested, with varying results. A discussion of this is presented in Appendix C.

C. Determining cohesive properties and validating the models

To test the models, determine the properties of the cohesive layer needed to implement CZM, and to allow for comparison against the benchmark solution presented by Krueger, 2015, the three models were first tested using a triangular cohesive law and the B-K mixed-mode fracture criterion, which is a built-in implementation of CZM in Abaqus. The pure mode I and pure mode II critical fracture toughness values, along with the experimentally determined exponent η, were obtained from Krueger's implementation of VCCT and are given in Table 3.

Cohesive strength and stiffness: To fully define a triangular cohesive law for a given material, two further parameters, the cohesive strength and stiffness, must be known. While these are usually determined experimentally, they are not known for these materials. Instead, parametric studies were conducted where

cohesive strength and stiffness were varied until the resultant load-displacement curves matched the benchmark solution reported by Krueger [20]. Since the ENF and MMB models share a common material, the studies were conducted using only the simpler DCB and ENF models. The range of strengths tested and the relationship between normal and shear strength were obtained from Xie et al., 2016 [4]. The stiffnesses tested were generally high to hold the two faces of the cohesive element together with little deformation in the elastic range. Results are presented in Fig. 7 to Fig. 10.

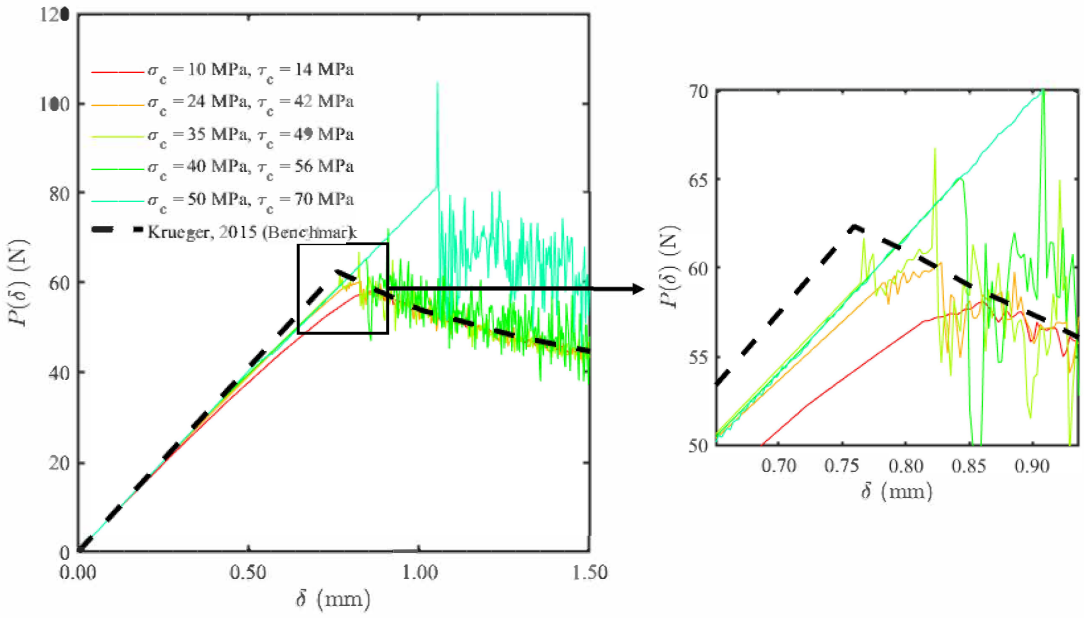

Fig. 7 Effect of cohesive strength on DCB load-displacement curve, for $K_I = K_{II} = K_{III} = 2 \times 10^5$ N/mm

In the DCB model, results of the parametric studies show that only for cohesive strengths below σ_c = 50 MPa, τ_c = 70 MPa does the load-displacement curve converge to the benchmark solution and remain stable at higher displacements. However, as cohesive strength increases, the peak load increases and the pre-peak response converges to the benchmark solution, becoming increasingly linear. Xie et al., 2016 [4] found that cohesive strength does not influence the post-peak response in DCB. Indeed, it does not affect the shape of the post peak response; however, higher strengths were observed to lead to greater instability and oscillations. This instability may be due to the very high initial elastic stiffness used [4]. To minimize post-peak oscillations and best capture the peak, cohesive strengths of σ_c = 24 MPa, τ_c = 42 MPa were selected for the DCB model. Results of the parametric studies for cohesive stiffness in DCB show no effect on the load-displacement curve. Thus, a stiffness of $K_I = K_{II} = K_{III} = 2 \times 10^5$ N/mm was arbitrarily selected.

In the ENF model, changing the cohesive strength was found to have the same effect as in the DCB model, with a lower strength contributing to a softening of the pre-peak response and a lowering of the peak, but also to smaller post-peak oscillations. To balance these factors, cohesive strengths of σ_c = 50 MPa, τ_c = 70 MPa were selected for the ENF and MMB models. This is justified since a different material was used for the ENF and MMB plies compared to DCB. Finally, in the ENF model, as before, increasing the cohesive stiffness was found not to change the pre- or post-peak load-displacement response, though the highest stiffness tested had the lowest oscillations post-peak. This stiffness, $K_I = K_{II} = K_{III} = 1 \times 10^6$ N/mm, was selected for the ENF and MMB models.

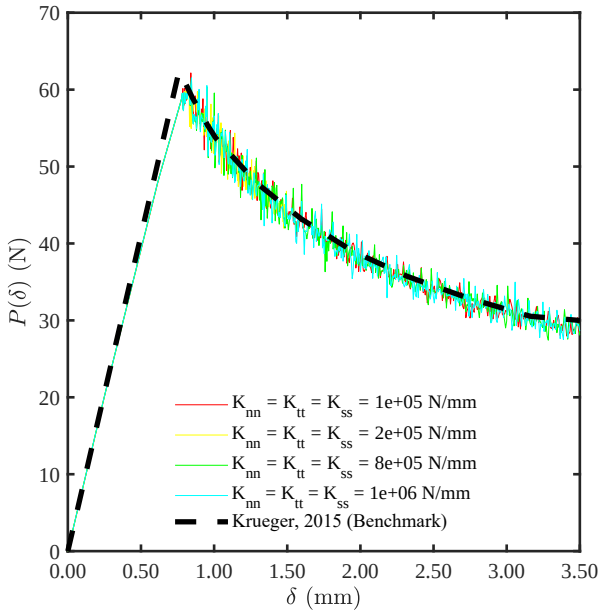

Fig. 8 Effect of cohesive stiffness on DCB load-displacement curve, for σ_c = 24 MPa, τ_c = 42 MPa

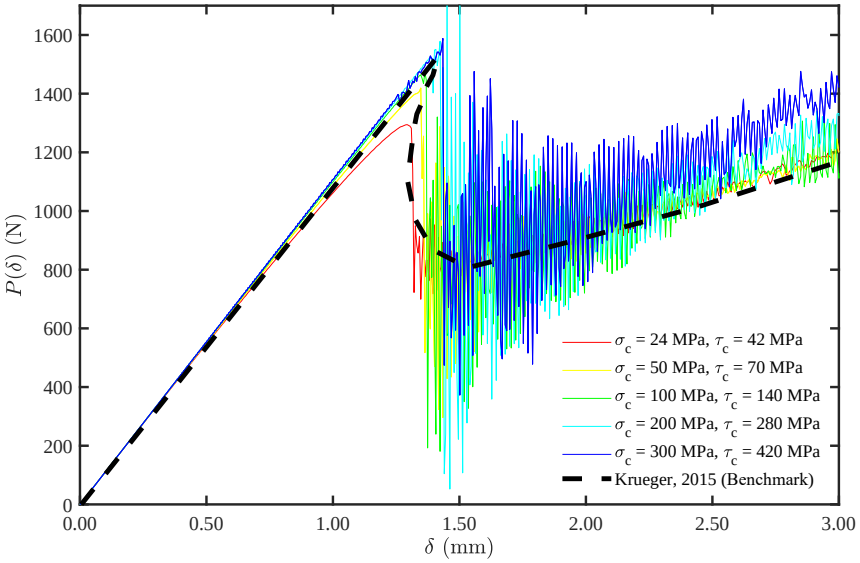

Fig. 9 Effect of cohesive strength on ENF load-displacement curve, for $K_I = K_{II} = K_{III} = 1 \times 10^6$ N/mm. The ENF model shares the same material as the MMB model.

The final cohesive properties, as reported by Krueger, 2015 [20] or determined through the above parametric studies, are given in Table 3. Visualizations of the deformed specimens, computed in Abaqus/Explicit using these cohesive properties, are given in Fig. 11. These show each specimen behaving as expected, with deformation visually similar to that observed in experiments [21, 29] and numerical studies from literature [10, 12, 20].

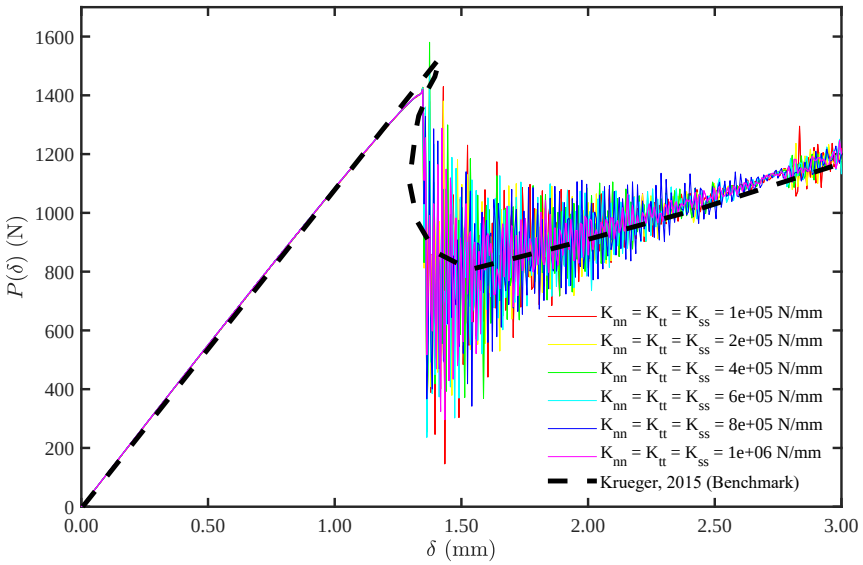

Fig. 10 Effect of cohesive stiffness on ENF load-displacement curve, for σ_c = 50 MPa, τ_c = 70 MPa. The ENF model shares the same material as the MMB model.

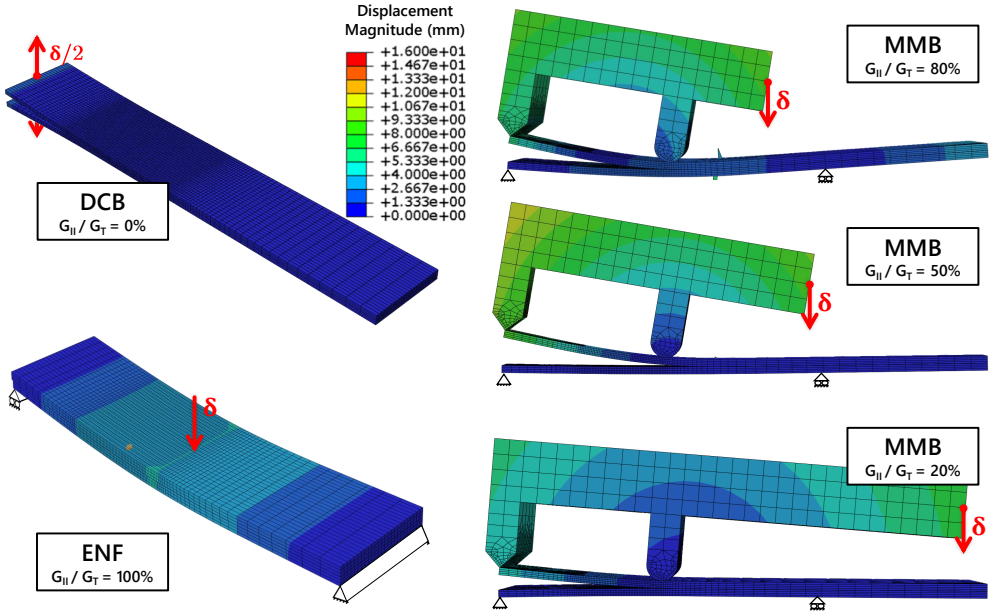

Fig. 11 Deformed 3D models of each test, with shading corresponding to the local displacement (in mm) of the ply material or loading arm.

Table 3 Final cohesive properties for each model, provided by Krueger et al. or determined through parametric studies.

Cohesive Property	DCB (T300/1076)	ENF/MMB (IM7/8552)
Density (tonne mm^{-3})	$\rho_c = 1.5 \times 10^{-9}$	$\rho_c = 1.5 \times 10^{-9}$
Cohesive Strength (MPa)	$\sigma_c = 24$ $\tau_c = 42$	$\sigma_c = 50$ $\tau_c = 70$
Cohesive Stiffness (N/mm)	$K_{\mathrm{I}} = K_{\mathrm{II}} = K_{\mathrm{III}} = 2 \times 10^5$	$K_{\mathrm{I}} = K_{\mathrm{II}} = K_{\mathrm{III}} = 1 \times 10^6$
Cohesive Thickness (mm)	$t = 0.002$	$t = 0.002$
B-K Criterion exponent	$\eta = 1.62$	$\eta = 2.1$
Fracture energy (kJ/m^2)	$G_{\mathrm{I}c} = 0.170$ $G_{\mathrm{II}c} = G_{\mathrm{III}c} = 0.494$	$G_{\mathrm{I}c} = 0.212$ $G_{\mathrm{II}c} = G_{\mathrm{III}c} = 0.774$

D. Defining a nonlinear cohesive traction-separation law and mixed-mode formulation

A custom cohesive traction-separation law with an alternative mixed-mode formulation was implemented, using a VUMAT user-defined subroutine to replace the built-in cohesive material definition in Abaqus. The alternative mixed-mode formulation represents a continuation of the work by Nguyen and Waas, 2021 [2] and relies on the definition of an effective separation. The formulation ensures that all tractions vanish simultaneously at the crack propagation and that when the crack is fully developed, the crack surface becomes traction-free.

For each pure-mode case, the elastic pre-peak response region of the cohesive traction separation law is modelled as linear with the penalty stiffness $K_{\mathrm{I}} = K_{\mathrm{II}} = K_{\mathrm{III}}$ up to the pure-mode cohesive strengths σ_c and τ_c determined in the previous section. The constitutive equation and initiation criterion are given in Eq. (6) and Eq. (7) below:

$$\begin{bmatrix} t_{\mathrm{I}} \\ t_{\mathrm{II}} \\ t_{\mathrm{III}} \end{bmatrix} = \begin{bmatrix} (1-d_{\mathrm{I}}) & 0 & 0 \\ 0 & (1-d_{\mathrm{II}}) & 0 \\ 0 & 0 & (1-d_{\mathrm{III}}) \end{bmatrix} \begin{bmatrix} K_{\mathrm{I}} & 0 & 0 \\ 0 & K_{\mathrm{II}} & 0 \\ 0 & 0 & K_{\mathrm{III}} \end{bmatrix} \begin{bmatrix} \delta_{\mathrm{I}} \\ \delta_{\mathrm{II}} \\ \delta_{\mathrm{III}} \end{bmatrix} \tag{6}$$

$$\left(\frac{\max(0, t_{\mathrm{I}}^*)}{\sigma_c}\right)^2 + \left(\frac{t_{\mathrm{II}}^*}{\tau_c}\right)^2 + \left(\frac{t_{\mathrm{III}}^*}{\tau_c}\right)^2 \geq 1 \tag{7}$$

When the initiation criterion is met at tractions $t_{\mathrm{I}}^*, t_{\mathrm{II}}^*$ and t_{III}^*, the cohesive response is governed by the separation components and non-dimensionalized softening functions f_i, modelled by a set of Bezier curves. It is assumed that compression does not affect the failure evolution. Fundamental material properties are the pure-mode fracture toughness values for each mode G_{ic}. G_{ic} is related to the area under the non-dimensionalized softening curve, $\overline{g}_{ic}^*$, via Eq. (8), from which the quantities of δ_i^f can be calculated. Final failure separations $\widehat{\delta}_i$ can be determined from Eq. (9) below.

$$F_i \; \delta_i^f \; \overline{g}_{ic}^* = G_{ic} - \frac{F_i^2}{2K_i} \tag{8}$$

$$\widehat{\delta}_i = \left|\delta_i^*\right| + \delta_i^f \text{ , where } i = \mathrm{I}, \mathrm{II}, \mathrm{III} \tag{9}$$

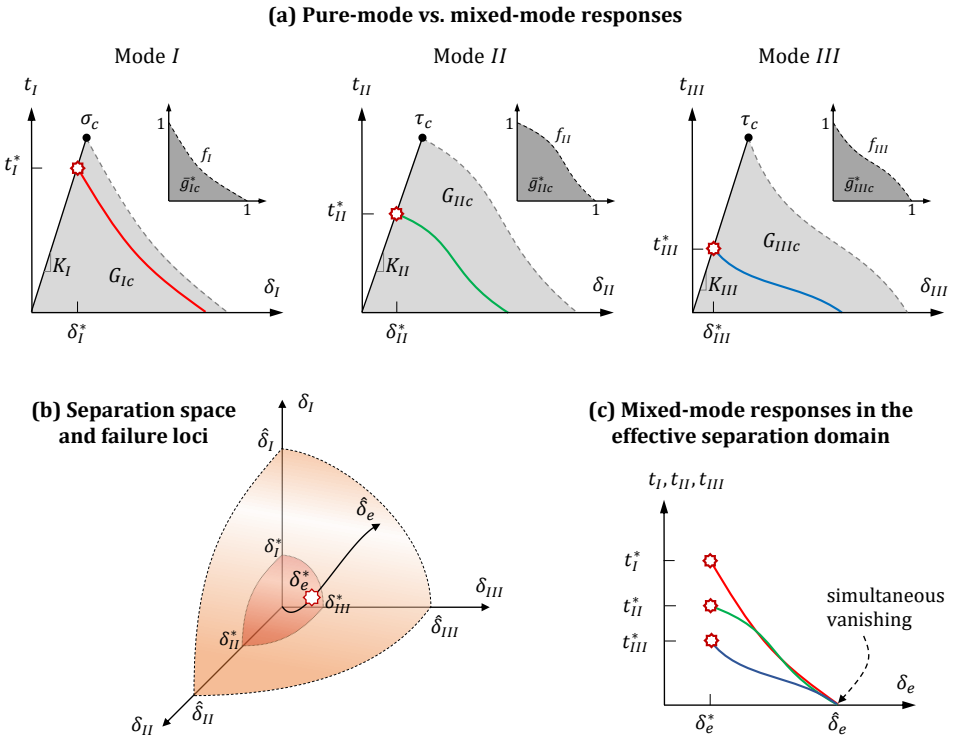

Fig. 12 Mixed-mode traction separation law for the cohesive behavior [2]. (a) Pure versus mixed-mode responses; (b) Separation space and failure loci; (c) Mixed-mode responses in the effective separation domain.

Under mixed-mode conditions, the softening of each mode is governed by the effective separation composed of the separation components, as given in Eq. (10), where mode I is chosen as the reference mode:

$$\delta_c = \sqrt{\max(0,\delta_{\mathrm{I}})^2 + \left(\frac{\widehat{\delta}_{\mathrm{I}}}{\widehat{\delta}_{\mathrm{II}}}\delta_{\mathrm{II}}\right)^2 + \left(\frac{\widehat{\delta}_{\mathrm{I}}}{\widehat{\delta}_{\mathrm{III}}}\delta_{\mathrm{III}}\right)^2} \tag{10}$$

The mixed-mode damage evolution is given in Eq. (11), where δ_e^* is the effective separation value at the initiation point and $\widehat{\delta}_e \equiv \widehat{\delta}_{\mathrm{I}}$, the final effective separation at complete failure.

$$d_i = 1 - \frac{\delta_e^*}{\delta_e}\overline{f}_i\left(\frac{\delta_e - \delta_e^*}{\widehat{\delta}_e - \delta_e^*}\right) \tag{11}$$

The proposed formulation ensures the simultaneous vanishing of all tractions. The loading/unloading behavior is governed by the effective separation increment, i.e. the damage variables remain constant if δ_e decreases. To prevent inter-penetration, a pristine penalty stiffness for mode I is imposed in case of compression: $d_{\mathrm{I}} = 0$ if $\delta_{\mathrm{I}} < 0$. It should be noted that friction is not yet considered in the current work but may be in future studies.

Practical verification in Abaqus: To implement the non-triangular pure mode cohesive laws, constitutive equations, and alternative mixed-mode formulation, the VUMAT takes in four Bezier curve control parameters

for each of the Mode I, II, and III cohesive softening laws along with several cohesive properties, including density, strength, stiffness, and critical fracture energy. The implementation of the subroutine for each model was verified by using the control parameters to replicate a linear softening law and comparing resultant load-displacement curves to those obtained with the triangular laws and B-K criterion with the exponent η reported by Krueger, 2015 or the Power Law with the exponent $\alpha = 1$. This comparison is given in Fig. 13.

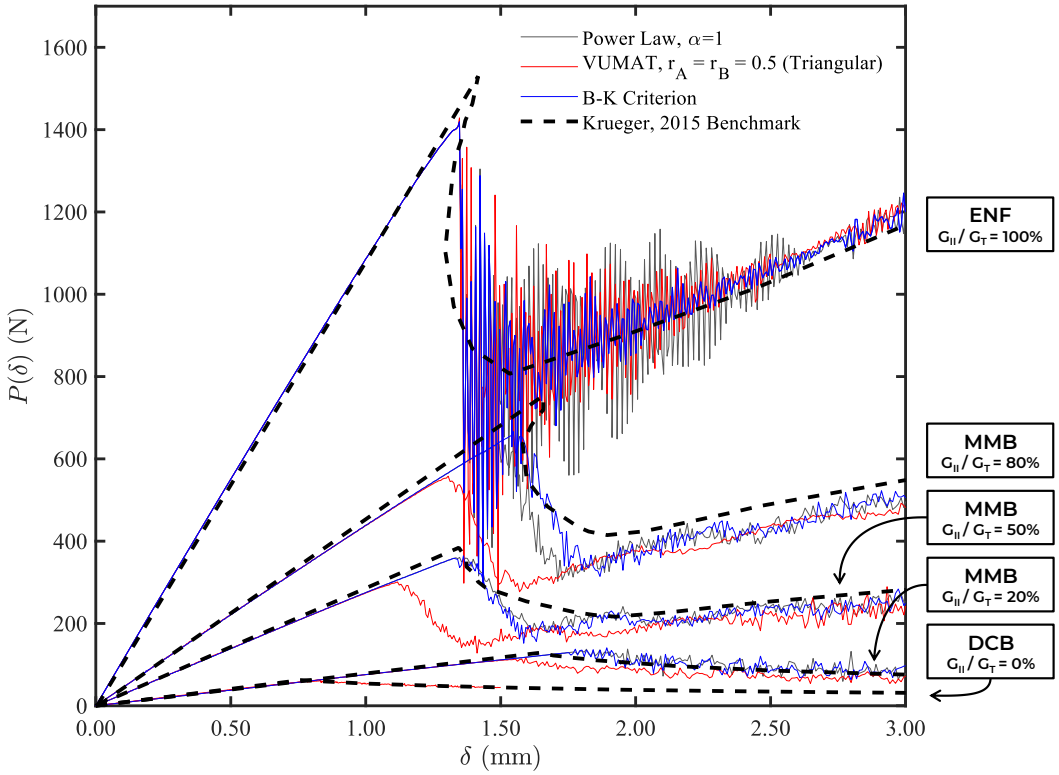

Fig. 13 Load-displacement curves for each of the six mode mixity ratios tested, comparing Krueger's benchmark curve (black, dashed), the solution obtained using the built-in Abaqus CZM implementation with the B-K criterion (blue) and power law ($\alpha = 1$, gray), and the solution obtained using the VUMAT with a triangular cohesive law (red).

While the versions of the models which implement the VUMAT (red) with the linear softening law return load-displacement curves similar to those of the built-in Abaqus implementation with the B-K criterion (blue) and power law (gray), Fig. 13 shows that the built-in implementation better matches the benchmark results. In general, the VUMAT model results in a pre- and post-peak slope that is identical to that of the built-in Abaqus and benchmark models but which fails to correctly capture the peak load. These results are closer to those obtained from the Power Law formulation than from those obtained from the B-K criterion implementation. This is expected as the benchmark study is based on the B-K criterion, as described above [20]. However, the standard cohesive implementations (both using the power law or the B-K criterion) are based on linear traction-separation softening laws. In reality, the material may not soften in a linear fashion. Indeed, the pure mode cohesive laws can be measured [3, 21, 23]. Thus, the above results show only that poor results are yielded when using strictly linear softening laws.

Softening law Bezier control parameter sweep: In this section, we study the mixed-mode responses when using non-linear softening laws along with the novel mixed-mode law by Nguyen and Waas, 2021 [2]. A parametric study was conducted to determine whether a set of four Bezier curve parameters can be chosen such that the peak load is successfully captured across each model. Each Bezier curve is parametrized by two

control variables, r_1 and r_2, as shown in Fig. 14 below.

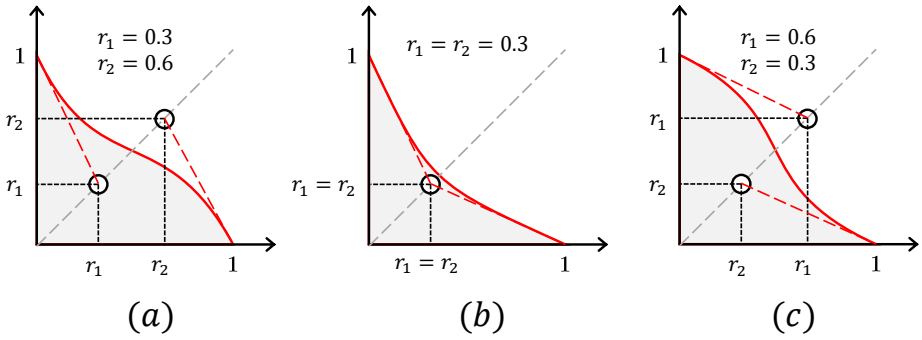

Fig. 14 Three examples of Bezier curves that can be generated using two parameters, r_1 and r_2 which lie along the x = y line.

The VUMAT allows the shape of the softening law after the peak to be defined arbitrarily, so parameters can be varied over the entire $[0, 1]$ range. However, experimentally measured cohesive traction-separation laws have been observed to always exhibit several key properties. Girolamo et al., 2015 observed that, after the peak, the cohesive softening law is consistently non-linear, and furthermore that in mode II laws it consistently begins and ends with a near-horizontal tangent [3]. For both mode I and mode II, they also determined that the final part of the softening law has a shallow slope that corresponds to the portion of the curve where the separation is so large that the ply interface can longer withstand the applied traction. Once the crack can no longer transfer load, the slope, represented by the stiffness, becomes zero; a smooth transition to zero-slope therefore requires a near-horizontal tangent. Hence, the range of parameters was reduced to cover only these cases. For the final part of the softening law to have a shallow slope, $r_2^{\mathrm{I,II}} < 0.5$ for both mode I and II (see Fig. 14 (b) and (c)). For the beginning of the mode II softening law to have a near-horizontal tangent, $r_1^{\mathrm{II}} > 0.5$ in that case only (see Fig.14 (c)).

Finally, in the cohesive laws observed by Girolamo et al., 2015 [3] and shown in Fig. 15 below, the softening law is symmetric. It is unclear whether this is always the case, however in the interest of further reducing the parameter space, the assumption was made that for mode I, $r_1^{\mathrm{I}} = r_2^{\mathrm{I}} = r_A$ and for mode II, $r_1^{\mathrm{II}} = 1 - r_2^{\mathrm{II}} = r_B$. This leads to the interesting restriction that for mode II, $\hat{\delta}_{\mathrm{II}}$ is always constant, since its parametrized Bezier curve is always symmetric about $r_2^{\mathrm{II}} = 1 - r_1^{\mathrm{II}}$, while for mode I, $\hat{\delta}_{\mathrm{I}}$ varies as a function of r_A. With these simplifications, only one Bezier parameter is required to characterize each of the cohesive laws in a cohesive material definition.

A set of example parametrizations of the cohesive laws observed by Girolamo et al., 2015 using a single Bezier parameter for each curve are presented in Fig. 15, alongside the experimental data. The cohesive laws were reconstructed from the non-dimensional Bezier curves using the cohesive material properties reported by Girolamo et al., $\sigma_c = 87.6$ MPa, $\tau_c = 47.5$ MPa, $K_{\mathrm{I}} = 12.4$ kN/mm, $K_{\mathrm{II}} = 4.3$ kN/mm, $G_{\mathrm{I}c} = 1.25$ kJ/m^2, and $G_{\mathrm{II}c} = 8.1$ kJ/m^2 (adhesive material). The figure shows that both for mode I and II, the parametrization can be accurately fit to the data, using $r_A = 0.11$ and $r_B = 0.72$.

Four uniformly spaced values were selected in the ranges identified for r_A and r_B. This gives the test matrix given in Table 4, to be tested over a range of mode mixity ratios. The Bezier curves which result from these parameters, along with the related cohesive laws for the ENF/MMB material, are shown in Fig. 16. Note that $r_A = r_B = 0.5$ represents linear softening laws.

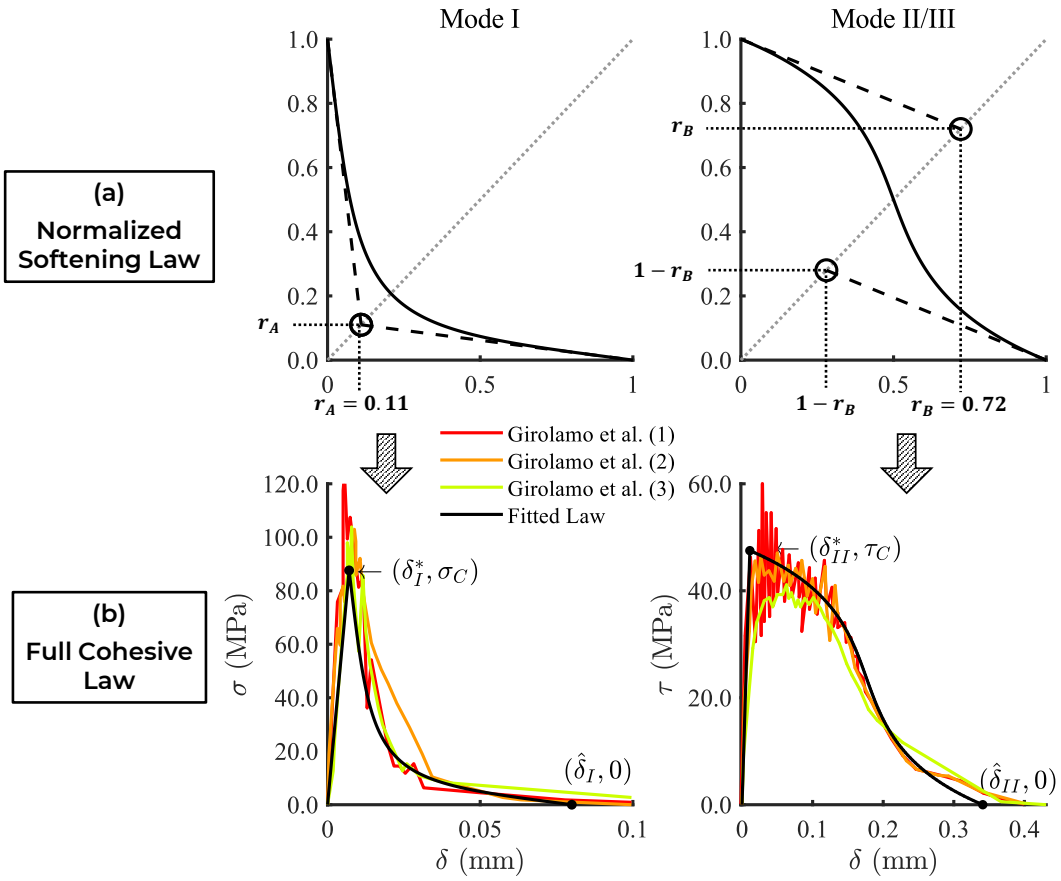

Fig. 15 (a) Mode I and II softening laws parametrized by Bezier curves with $r_A = 0.11, r_B = 0.72$. (b) Cohesive laws generated from the above Bezier curves and known cohesive properties, compared to experimental laws observed by Girolamo et al., 2015 [3].

Table 4 Test matrix showing combinations of Bezier curve parameters r_A and r_B tested in the parametric sweep. These were tested for each MMB mode mixity ratio.

	$r_B = 0.5$	$r_B = 0.633$	$r_B = 0.766$	$r_B = 0.9$
$r_A = 0.1$	•	•	•	•
$r_A = 0.233$	•	•	•	•
$r_A = 0.366$	•	•	•	•
$r_A = 0.5$	•	•	•	•

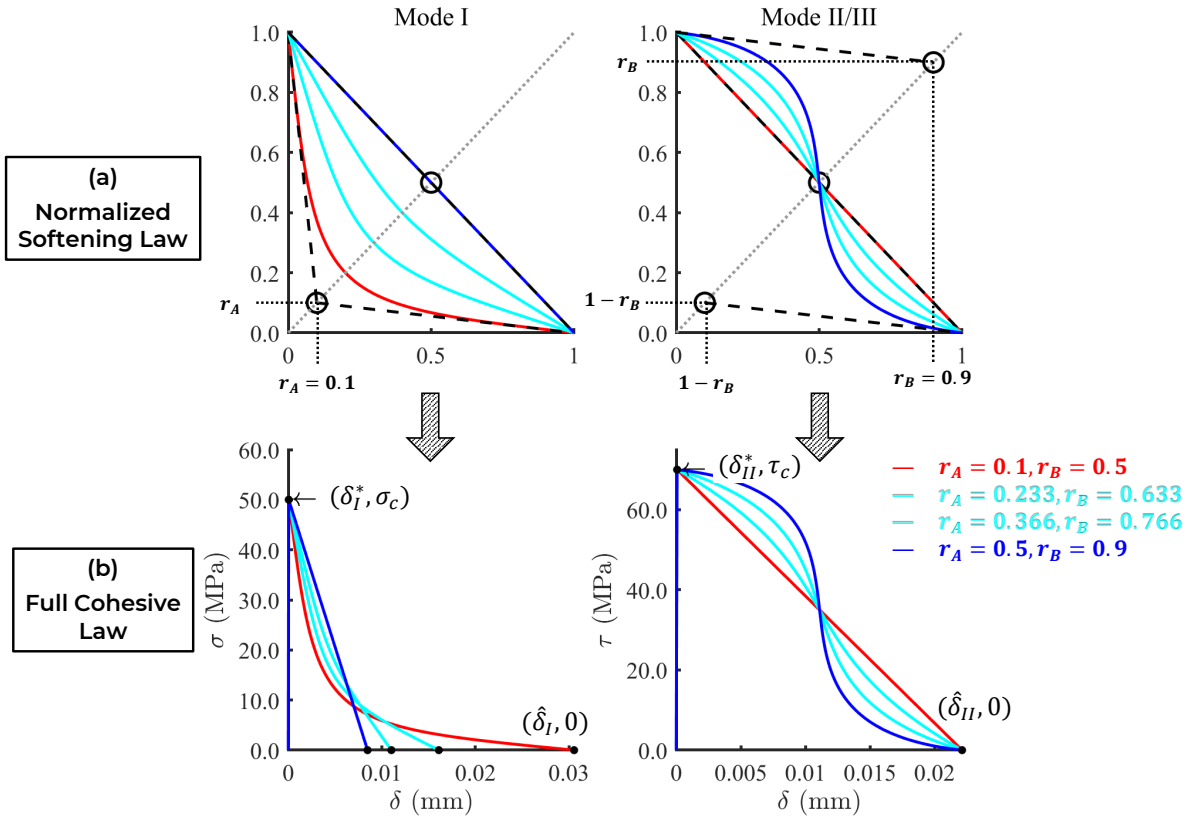

Fig. 16 (a) Set of distinct Bezier curves tested, where $r_A = 0.1, 0.233, 0.366, 0.5$ (Mode I), and $r_B = 0.5, 0.633, 0.766, 0.9$ (Mode II/III). Control points for red and blue curves are shown as empty circles. (b) Cohesive law corresponding to each Bezier curve, generated using known ENF/MMB cohesive properties. The area under each law is critical fracture energy, G_{ic}.

III. Results & Discussion

The results of the Bezier parametric studies for each of the MMB mixity ratios are presented in Fig. 17 to 22 below. For each, a plot showing the combined load-displacement curves for each parameter combination, of the built-in Abaqus implementation with the B-K criterion, and of Krueger's benchmark [20] is given. To evaluate the quality of the correlation between the Bezier parameter and the peak load, a normalized measurement of covariance called the Pearson Correlation Coefficient, ρ, was used, where $-1 \leq \rho \leq 1$. As $|\rho| \rightarrow 1$, the correlation improves.

Results for $G_{II}/G_T = 20\%$ are shown in Fig. 17 and 18. Fig. 17 shows distinct bands, representing a clustering curves with different r_B values but the same r_A value. Though the curves in these clusters are not identical, their peak load is very similar, indicating a weak dependence of the mode II Bezier parameter. This is confirmed by the correlations in Fig. 18, which show a correlation coefficient of only $\rho = 0.06$. On the other hand, the mode I parameter, r_A, has a high correlation coefficient of $\rho = -0.96$ and a slope of -74.19 N. Overall, the load-displacement curves from the models with the custom VUMAT implementation show a consistently smaller amplitude of oscillation that the models with the B-K criterion.

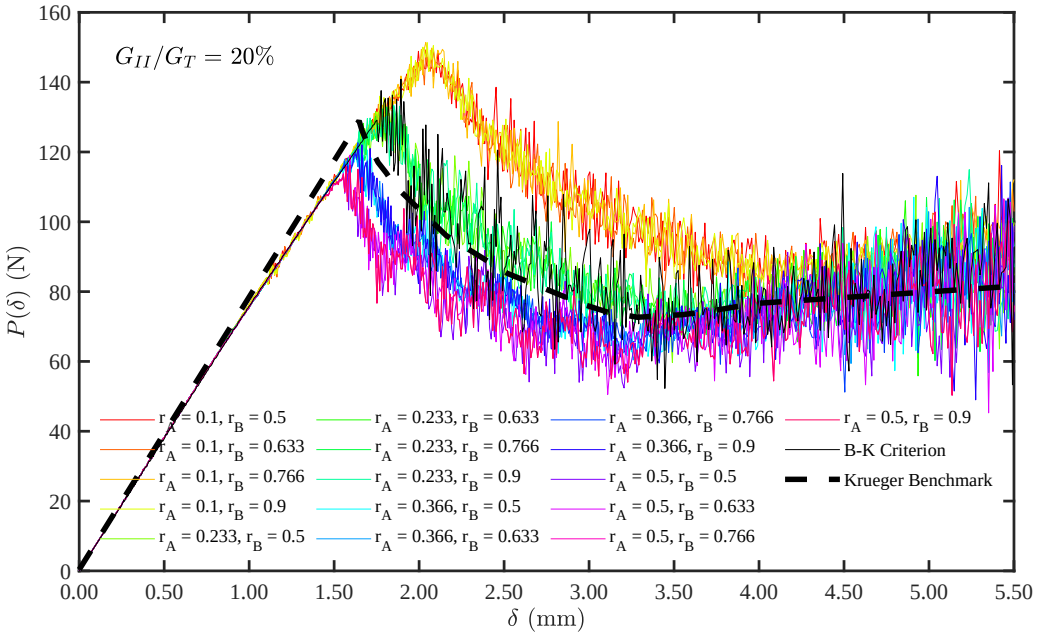

Fig. 17 Several MMB load-displacement curves showing the effect of varying r_A and r_B parameters with G_{II}/G_T = 20%.

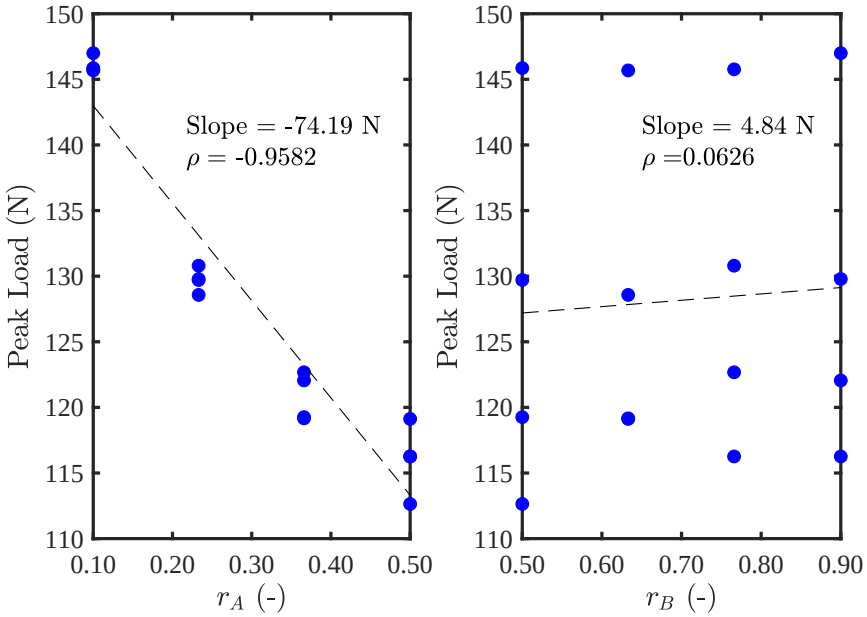

Fig. 18 Peak load as a function of the Bezier parameters for G_{II}/G_T = 20%, showing strong correlation between peak and r_A (left), and very little correlation between peak and r_B (right).

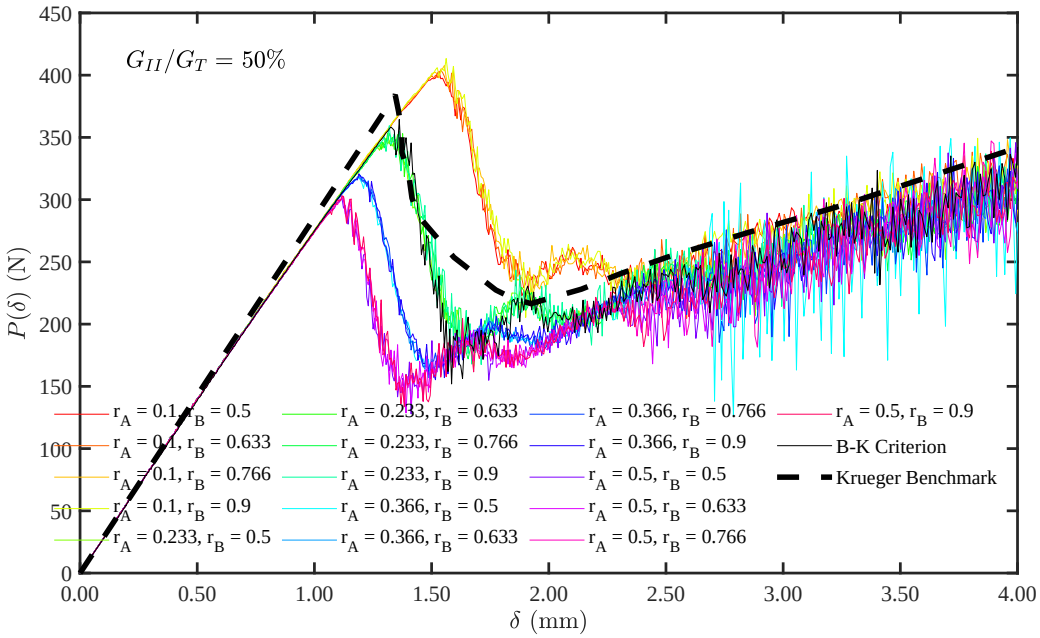

Fig. 19 Several MMB load-displacement curves showing the effect of varying r_A and r_B parameters with G_{II}/G_T = 50%.

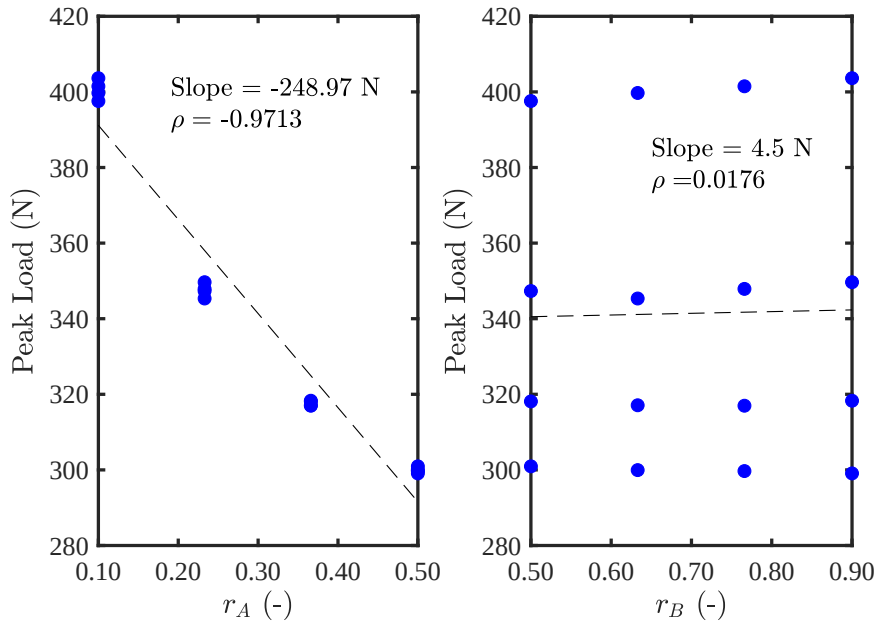

Fig. 20 Peak load as a function of the Bezier parameters for G_{II}/G_T = 50%, showing strong correlation between peak and r_A (left), and very little correlation between peak and r_B (right).

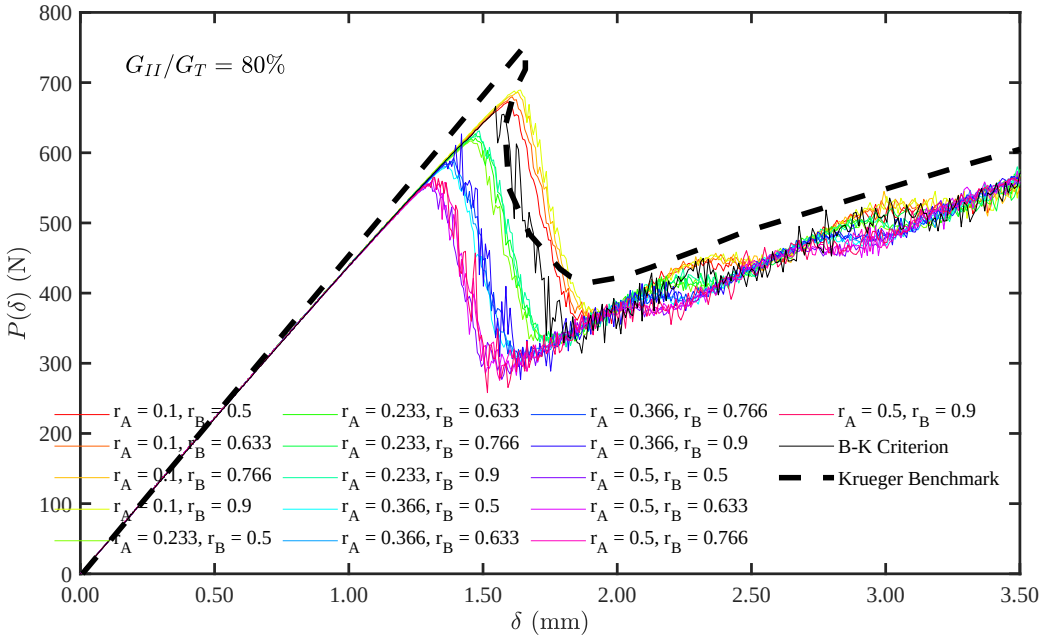

Fig. 21 Several MMB load-displacement curves showing the effect of varying r_A and r_B parameters with G_{II}/G_T = 80%.

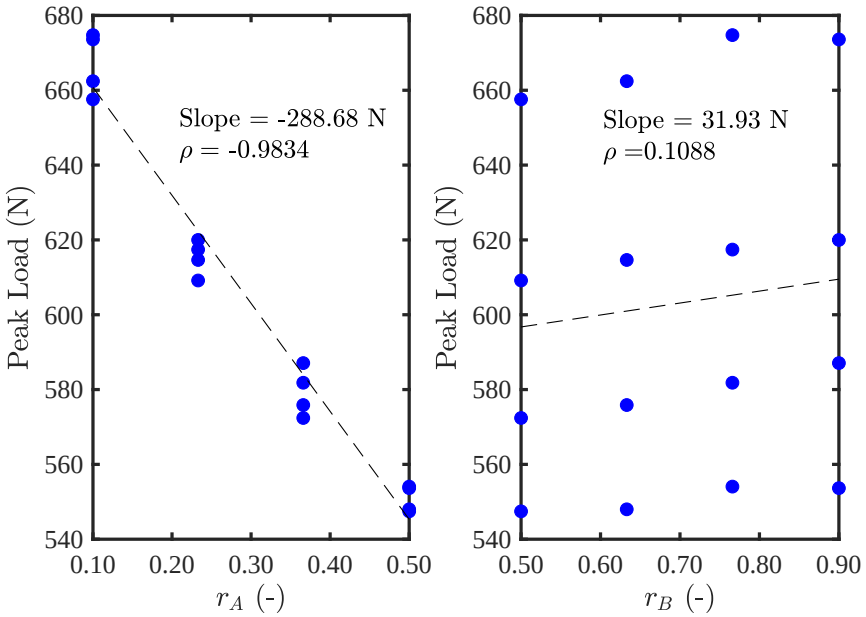

Fig. 22 Peak load as a function of the Bezier parameters for G_{II}/G_T = 80%, showing strong correlation between peak and r_A (left), and a slight correlation between peak and r_B (right).

Results for $G_{II}/G_T = 50\%$ are shown in Fig. 19 and Fig. 20. These show a very similar trend to $G_{II}/G_T = 20\%$, though the slope of the mode I correlation is steeper at -249 N with a correlation coefficient of $\rho = -0.97$, and the mode II correlation coefficient is even lower at $\rho = 0.02$. Here again, oscillations from the VUMAT models have a smaller amplitude than the B-K criterion solution.

Results for $G_{II}/G_T = 80\%$ are shown in Fig. 21 and Fig. 22. These are again show the same features as before. For the mode I correlation, $\rho = -0.98$ and the slope is -289 N. However, this time the mode II correlation coefficient is a statistically significant $\rho = 0.10$. This suggests that there may indeed be a weak correlation between the mode II softening law shape and the peak load, which is expected for a mixed-mode condition with a high proportion of mode II. This unexpected weak correlation suggests that the restrictions placed on the shape of the Mode II softening Bezier curve may have been too strict, as enforcing symmetry about $r_2^{II} = 1 - r_1^{II} = 1 - r_B$ leads to constraining $\hat{\delta}_{II}$ to a constant value for all r_B values.

Finally, the influence of the nonlinear softening law on the DCB and ENF models ($G_{II}/G_T = 0$ and 100%, respectively) was studied, with results given in Fig. 23. Though the different ply and cohesive material in the DCB test prevents a direct comparison, these results are consistent with those from the MMB tests. Little-to-no dependence on the shape of the mode II law is observed for the ENF model (this again suggests the constraints on the mode II control parameters may be too strict). Conversely, a dependence is observed for mode I in DCB, where the law with nonlinear softening undershoots the expected peak load.

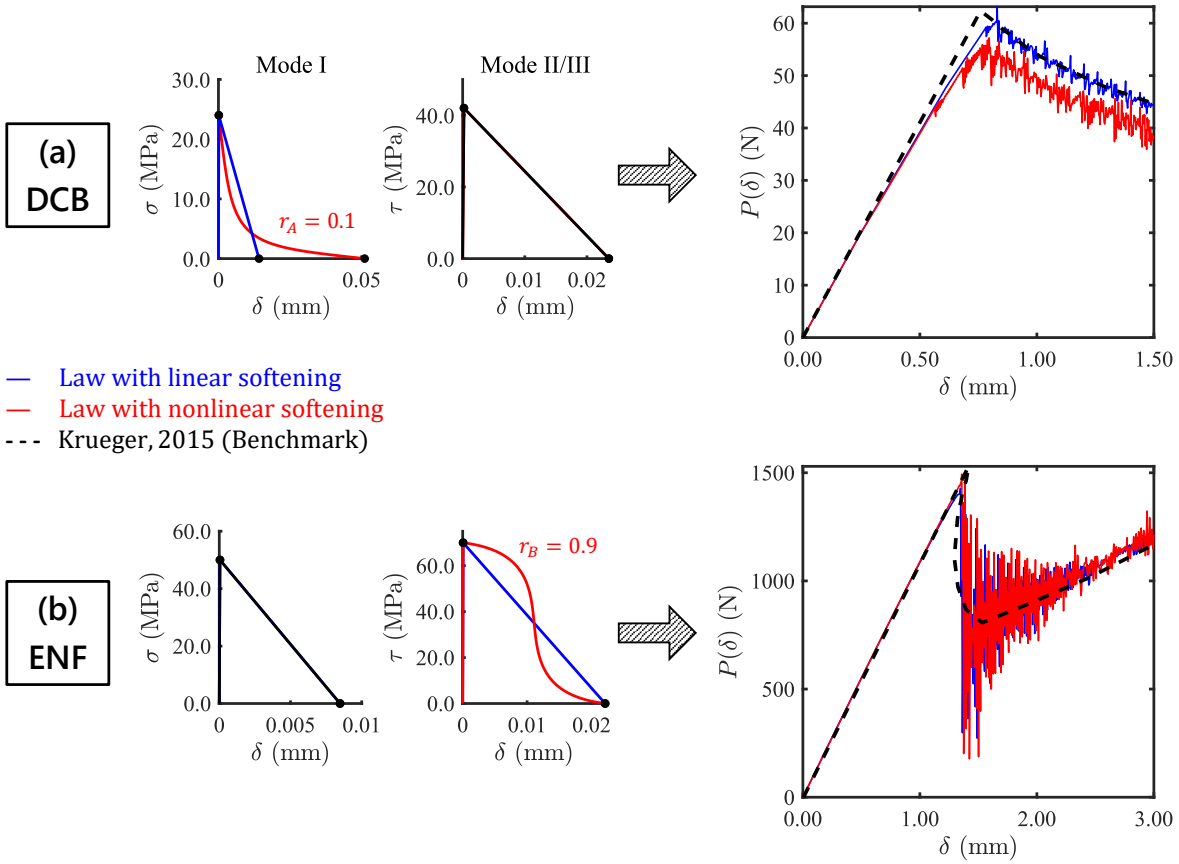

Fig. 23 (a) Load-displacement curves for the DCB model with a linear (blue) and nonlinear (red) mode I softening law, for $r_A = 0.1$. (b) Load-displacement curves for the ENF model with a linear (blue) and nonlinear (red) mode II softening law, for $r_B = 0.9$.

Ultimately, no single combination of r_A and r_B parameters exists that gives a peak load exactly equal to the peak load from the simulation with the B-K criterion across each of the mode mixity ratios. For this to be true, $r_A = 0.288$ when $G_{II}/G_T = 20\%$; $r_A = 0.233$ when $G_{II}/G_T = 50\%$; and $r_A = 0.077$ when $G_{II}/G_T = 80\%$. r_B parameters were not considered due to their weak correlation. Using the nearest or best parameter combination of $r_A = 0.233$, $r_B = 0.9$ gives relatively good results across all mixity ratios as shown in Fig. 24.

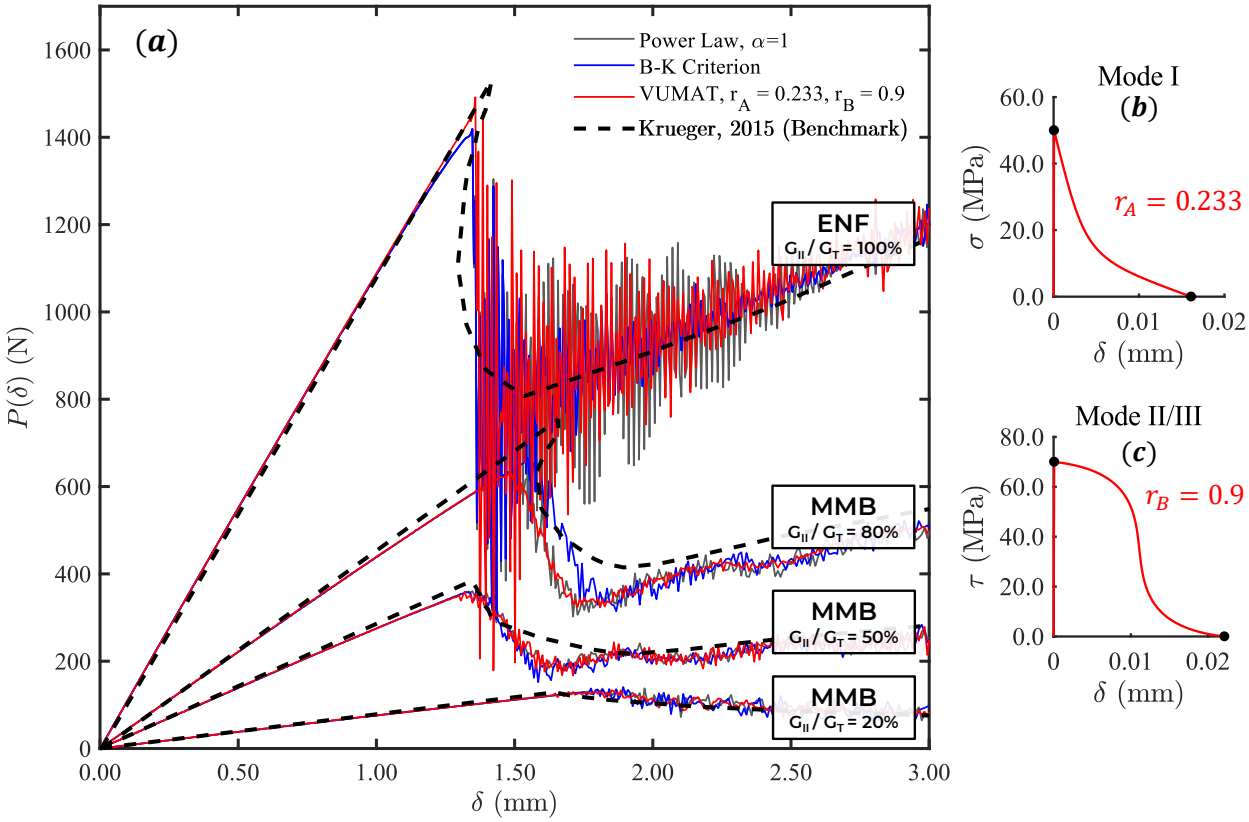

Fig. 24 (a) Load-displacement curves for a range of mode mixity ratios tested, comparing Krueger's benchmark curve (black, dashed), the solution obtained using the built-in Abaqus CZM implementation with the B-K criterion (blue) and power law ($\alpha = 1$, gray), and the solution obtained using the VUMAT with the "best" set of Bezier curve parameters (red). These curves for mode I (b) and mode II/III (c) are shown.

Furthermore, Fig. 24 shows that while the best set of Bezier parameters do not consistently yield a curve that reaches the same peak load as the B-K criterion, they do yield a curve that very closely matches that obtained using the power law with $\alpha = 1$ and correctly capture the post-peak slope, both before and after the post-peak inflection point. Also interesting is the observation that the pre-peak prediction for ENF case by the novel mixed-mode law comes closest to the benchmark curve. This may be attributed to the fact that the mode II traction-separation law softens slowly at the start with the Bezier parameter $r_B = 0.9$.

IV. Conclusions

In this study, the development and validation of DCB, ENF, and several MMB models for the simulation of quasi-static delamination propagation in Abaqus/Explicit was discussed in detail. Parametric studies were conducted to determine the cohesive strength and stiffness which yielded the best results for each material tested, as compared to a series of benchmark results obtained from literature [20]. Once validated, the cohesive material definition was replaced with a user-defined subroutine that allows for non-linear cohesive traction-separation softening laws defined by a Bezier curve to be used, along with custom constitutive equations and mixed-mode formulation [2]. Load-displacement curves for each loading condition were obtained using this custom formulation and compared to results using the B-K criterion and Power Law, first with a triangular law and then with a range of Bezier curve parameters. Results show that when a triangular law is used, the custom formulation does not correctly capture the peak load, but that this can be improved significantly by using a non-linear softening law which better corresponds to experimentally observed mode I and mode II cohesive laws. While a single set of Bezier curve parameters which gives perfect peak load results across all mode mixity ratios could not be obtained, this study demonstrated that the best set of parameters tested produced results which were on-par with those obtained through the Power Law formulation with $\alpha = 1$, though it fails to capture the peak load as consistently as models implementing the Benzeggagh-Kenane (B-K) criterion.

Further studies are required to characterize the influence of the Bezier curve parameters with greater granularity, to potentially obtain an empirical relationship between each curve parameter and the peak load observed. In future work, constraints should be loosened on the Bezier parameters for the Mode II softening law, so as to better characterize the potential relationship and influence on the delamination growth prediction.

References

[1] Camanho, P. P., Davila, C. G., and de Moura, M. F., "Numerical Simulation of Mixed-Mode Progressive Delamination in Composite Materials," *Journal of Composite Materials*, Vol. 37, No. 16, 2003, pp. 1415–1438. https://doi.org/10.1177/0021998303034505.

[2] Nguyen, M. H., and Waas, A. M., "Modeling delamination migration in composite laminates using an enhanced semi-discrete damage model (eSD2M)," *International Journal of Solids and Structures (In Review)*, 2021.

[3] Girolamo, D., Davila, C. G., Leone, F. A., and Lin, S.-Y., "Cohesive Laws and Progressive Damage Analysis of Composite Bonded Joints, a Combined Numerical/Experimental Approach," *56th AIAA/ASCE/AHS/ASC Structures, Structural Dynamics, and Materials Conference*, 2015. https://doi.org/10.2514/6.2015-1578, URL https://arc.aiaa.org/doi/abs/10.2514/6.2015-1578.

[4] Xie, J., Waas, A. M., and Rassaian, M., "Closed-form solutions for cohesive zone modeling of delamination toughness tests," *International Journal of Solids and Structures*, Vol. 88-89, 2016, pp. 379–400. https://doi.org/10.1016/j.ijsolstr.2015.12.025, URL https://www.sciencedirect.com/science/article/pii/S0020768315005259.

[5] Elices, M., Guinea, G. V., Gómez, J., and Planas, J., "The cohesive zone model: advantages, limitations and challenges," *Engineering Fracture Mechanics*, Vol. 69, No. 2, 2002, p. 137–163. https://doi.org/10.1016/s0013-7944(01)00083-2.

[6] Bazilevs, Y., Pigazzini, M. S., Ellison, A., and Kim, H., "A new multi-layer approach for progressive damage simulation in composite laminates based on isogeometric analysis and Kirchhoff–Love shells. Part I: basic theory and modeling of delamination and transverse shear," *Computational Mechanics*, Vol. 62, No. 3, 2018, pp. 563–585. https://doi.org/10.1007/s00466-017-1513-1, URL https://doi.org/10.1007/s00466-017-1513-1.

[7] Zhu, M., Gorbatikh, L., and Lomov, S. V., "An Incremental Cohesive Law for Delamination Under a Mixed Mode Loading," *Frontiers in Materials*, Vol. 7, 2020, p. 366. https://doi.org/10.3389/fmats.2020.572995, URL https://www.frontiersin.org/article/10.3389/fmats.2020.572995.

[8] Joki, R., Grytten, F., Hayman, B., and Sørensen, B., "A mixed mode cohesive model for FRP laminates incorporating large scale bridging behaviour," *Engineering Fracture Mechanics*, Vol. 239, 2020, p. 107274. https://doi.org/10.1016/j.engfracmech.2020.107274, URL https://www.sciencedirect.com/science/article/pii/S0013794420308572.

[9] Turon, A., Camanho, P., Costa, J., and Dávila, C., "A damage model for the simulation of delamination in advanced composites under variable-mode loading," *Mechanics of Materials*, Vol. 38, No. 11, 2006, pp. 1072–1089. https://doi.org/10.1016/j.mechmat.2005.10.003, URL https://www.sciencedirect.com/science/article/pii/S0167663605002000.

[10] De Carvalho, N., Czabaj, M., and Ratcliffe, J., "Piecewise-linear generalizable cohesive element approach for simulating mixed-mode delamination," *Engineering Fracture Mechanics*, Vol. 242, 2021, p. 107484. https://doi.org/10.1016/j.engfracmech.2020.107484, URL https://www.sciencedirect.com/science/article/pii/S0013794420310468.

[11] Hu, P., Pulungan, D., and Lubineau, G., "An enriched cohesive law using plane-part of interfacial strains to model intra/inter laminar coupling in laminated composites," *Composites Science and Technology*, Vol. 200, 2020, p. 108460. https://doi.org/10.1016/j.compscitech.2020.108460, URL https://www.sciencedirect.com/science/article/pii/S0266353820322508.

[12] Mi, Y., Crisfield, M. A., Davies, G. A. O., and Hellweg, H. B., "Progressive Delamination Using Interface Elements," *Journal of Composite Materials*, Vol. 32, No. 14, 1998, pp. 1246–1272. https://doi.org/10.1177/002199839803201401, URL 10.1177/002199839803201401.

[13] Azab, M., Parry, G., and Estevez, R., "An analytical model for DCB/wedge tests based on Timoshenko beam kinematics for accurate determination of cohesive zone lengths," *International Journal of Fracture*, Vol. 222, No. 1, 2020, pp. 137–153. https://doi.org/10.1007/s10704-020-00438-2, URL 10.1007/s10704-020-00438-2.

[14] Rybicki, E., and Kanninen, M., "A finite element calculation of stress intensity factors by a modified crack closure integral," *Engineering Fracture Mechanics*, Vol. 9, 1977, pp. 931–938.

[15] Rinderknecht, S., and Kröplin, B., "Calculation of Delamination Growth With Fracture and Damage Mechanics," *Recent Developments in Finite Element Analysis*, International Center for Numerical Methods in Engineering (CIMNE), 1994, Chap. 11.

[16] Dugdale, D., "Yielding of steel sheets containing slits," *Journal of Mechanics Physics of Solids*, Vol. 8, No. 2, 1960, pp. 100–104. https://doi.org/10.1016/0022-5096(60)90013-2.

[17] ASTM International (American Society for Testing and Materials), "Standard Test Method for Mode I Interlaminar Fracture Toughness of Unidirectional Fiber-Reinforced Polymer Matrix Composites," *Book of Standards*, Vol. 15.03, No. ASTM D5528-13, 2013. URL https://www.astm.org/Standards/D5528.htm.

[18] ASTM International (American Society for Testing and Materials), "Standard Test Method for Determination of the Mode II Interlaminar Fracture Toughness of Unidirectional Fiber-Reinforced Polymer Matrix Composites," *Book of Standards*, Vol. 15.03, No. ASTM D7905 / D7905M-19e1, 2019. URL https://www.astm.org/Standards/D7905.htm.

[19] ASTM International (American Society for Testing and Materials), "Standard Test Method for Mixed Mode I-Mode II Interlaminar Fracture Toughness of Unidirectional Fiber Reinforced Polymer Matrix Composites," *Book of Standards*, Vol. 15.03, No. ASTM D6671 / D6671M - 19, 2019. URL https://www.astm.org/Standards/D6671.htm.

[20] Krueger, R., "A summary of benchmark examples to assess the performance of quasi-static delamination propagation prediction capabilities in finite element codes," *Journal of Composite Materials*, Vol. 49, No. 26, 2015, pp. 3297–3316. https://doi.org/10.1177/0021998314561812, URL https://doi.org/10.1177/0021998314561812.

[21] Zobeiry, N., "Extracting the strain - softening response of composites using full - field displacement measurement," Ph.D. thesis, University of British Columbia, 2010. https://doi.org/10.14288/1.0062622.

[22] Jirásek, M., and Patzák, B., "Consistent tangent stiffness for nonlocal damage models," *Computers & Structures*, Vol. 80, 2002. https://doi.org/10.1016/S0045-7949(02)00078-0.

[23] Nguyen, N., and Waas, A., "Nonlinear, finite deformation, finite element analysis," *Zeitschrift für angewandte Mathematik und Physik*, Vol. 67, 2016. https://doi.org/10.1007/s00033-016-0623-5.

[24] Wu, E. M., and Reuter, R. C., "Crack Extension in Fiberglass Reinforced Plastics," Tech. Rep. 275, University of Illinois, Department of Theoretical and Applied Mechanics, Urbana, IL, 1965. URL https://apps.dtic.mil/sti/citations/AD0613576, commissioned by the U.S. Bureau of Naval Weapons.

[25] Benzeggagh, M., and Kenane, M., "Measurement of mixed-mode delamination fracture toughness of unidirectional glass/epoxy composites with mixed-mode bending apparatus," *Composites Science and Technology*, Vol. 56, No. 4, 1996, pp. 439–449. https://doi.org/10.1016/0266-3538(96)00005-X.

[26] Reeder, J. R., "Refinements to the Mixed-Mode Bending Test for Delamination Toughness," *Journal of Composites Technology & Research*, Vol. 25, 2000, pp. 1–5.

[27] Underwriters Laboratories (UL), "Epoxy Typical Properties Generic Epoxy," Webpage, 2021. URL https://plastics.ulprospector.com/generics/13/c/t/epoxy-properties-processing, retrieved from the UL Prospector Property Database.

[28] MatWeb, "Steels, General Properties," Webpage, 1996. Retrieved from the MatWeb Material Property Database.

[29] Abd Rased, M., and Yoon, S., "Experimental study on effects of asymmetrical stacking sequence on carbon fiber/epoxy filament wound specimens in DCB, ENF, and MMB tests," *Composite Structures*, Vol. 264, 2021, p. 113749. https://doi.org/10.1016/j.compstruct.2021.113749.

Appendices

Appendix A: MMB lever length and mixity ratio

The length, c, of the lever arm in the MMB test apparatus determines the mode mixity ratio, G_{II}/G_T, with which the specimen is loaded when a displacement is applied to the end of the lever. Camanho et al., 2003 gives the following relationship, Eq. (12), between the desired ratio and c, where ℓ is the half-length of the specimen [1].

$$c = \frac{\ell\left(\frac{1}{2}\sqrt{3\left(\frac{1-(G_{II}/G_T}{G_{II}/G_T)}\right)+1}\right)}{3-\frac{1}{2}\sqrt{\frac{1-(G_{II}/G_T)}{G_{II}/G_T}}} \tag{12}$$

For example, for a specimen length of 100.8 mm and $G_{II}/G_T = 20\%$, $c = 92.9$ mm; for $G_{II}/G_T = 50\%$, $c = 41.3$ mm; and for $G_{II}/G_T = 80\%$, $c = 27.3$ mm.

Appendix B: Effect of cohesive thickness on load-displacement behavior

The influence of using a cohesive layer with a geometric thickness of 0.002 mm, as compared to a manually-defined zero-thickness cohesive layer was studied. A comparison of the load-displacement curve for both scenarios in the ENF model is highlighted in Fig. 25 below. Results show that the load-displacement response is identical in both cases, except for larger oscillations when a zero-thickness layer is used.

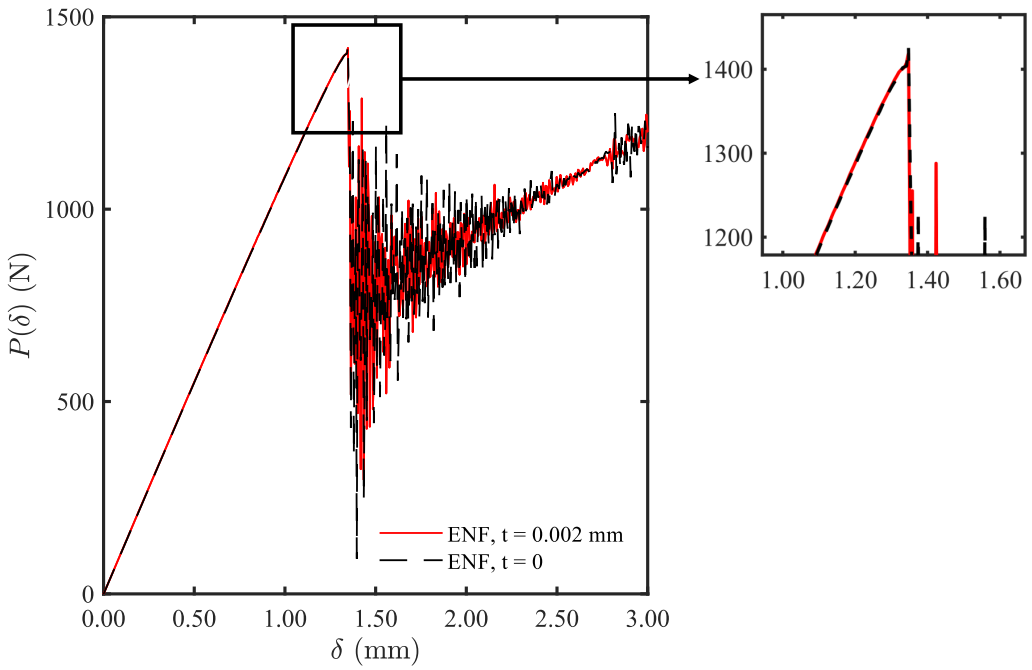

Fig. 25 Comparison of ENF load-displacement curves for a small, discrete cohesive thickness of 0.002 mm vs. a zero-thickness layer. Responses identical except for larger oscillations in the latter case.

Appendix C: Mass scaling study

A stable time increment of $\Delta t = 1 \times 10^{-6}$ s was used throughout this project. Though a smaller time increment of $\Delta t = 1 \times 10^{-7}$ s was tested to decrease the amplitude of oscillations in the solution, this simulation exceeded the maximum run time of 10 hours and was therefore not used. A larger time increment of $\Delta t = 1 \times 10^{-5}$ s was also tested. The figure below shows a comparison between a time increment of $\Delta t = 1 \times 10^{-5}$ s and $\Delta t = 1 \times 10^{-6}$ s. The former had an unacceptable amplitude of oscillations after the peak, as shown in Fig. 26, so the latter time increment was chosen for this project.

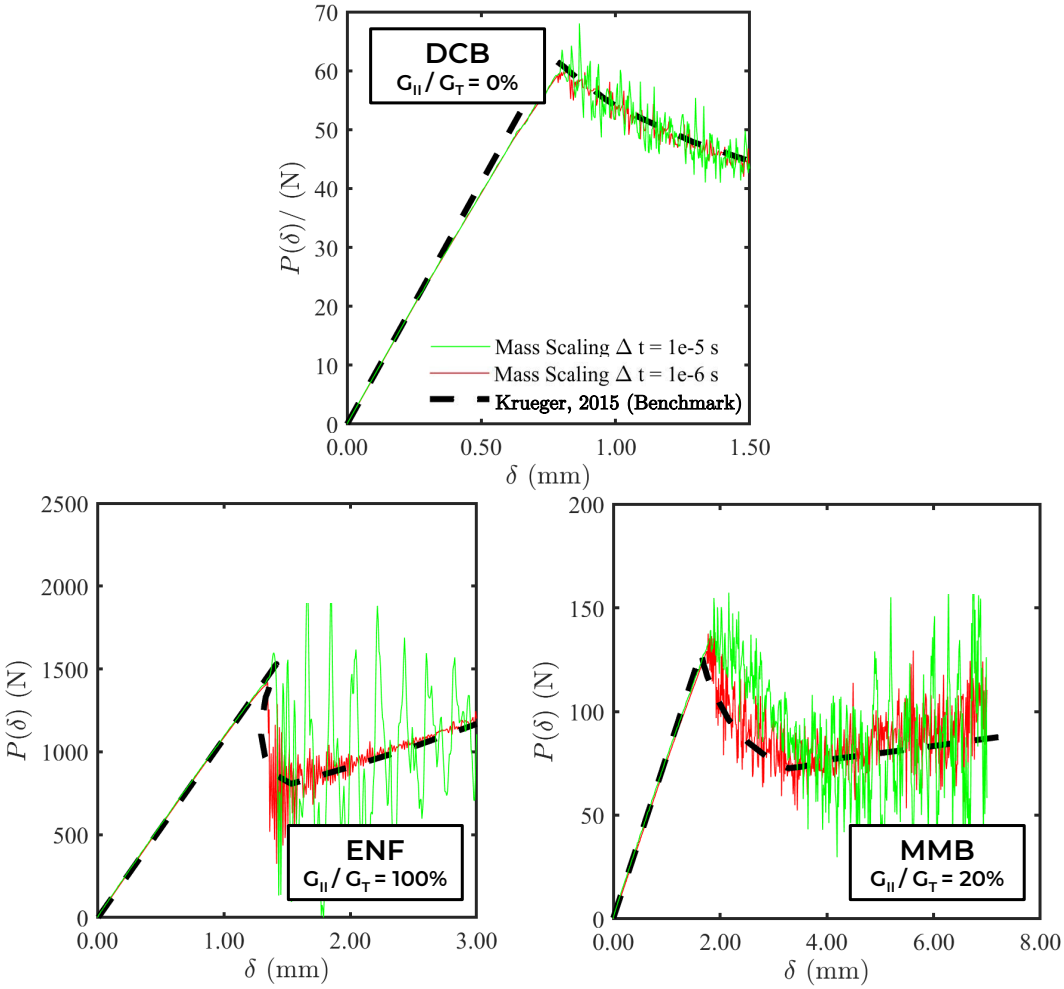

Fig. 26 Comparison of load-displacement curves between a stable time increment of $\Delta t = 1 \times 10^{-5}$ s and $\Delta t = 1 \times 10^{-6}$ s, showing significantly greater oscillations of growing amplitude in the former case.